Nucleation and growth of oxide particles on a binary Fe-Mn (1 wt. %) alloy during annealing

L. Gong, N. Ruscassier, Pascal Chrétien, P. Haghi-Ashtiani, L. Yedra, M.-L. Giorgi

Nucleation and growth of oxide particles on a binary Fe-Mn (1 wt. %) alloy during annealing

L. Gong [1], N. Ruscassier [1, *], P. Chrétien [2], P. Haghi-Ashtiani [3], L. Yedra[3], M.-L. Giorgi [1, *]

[1] LGPM, CentraleSupélec, Université Paris Saclay, 3 rue Joliot-Curie, 91192 Gif-sur-Yvette cedex, France.

[2] GeePS, CentraleSupélec, Université Paris Saclay, 11 rue Joliot-Curie, 91192 Gif-sur-Yvette cedex, France.

[3] MSSMat, CNRS, CentraleSupélec, Université Paris Saclay, 3 rue Joliot-Curie, 91192 Gif-sur-Yvette cedex, France.

[*] Corresponding authors. Nathalie.ruscassier@centralesupelec.fr (N. Ruscassier), marie-laurence.giorgi@centrealesupelec.fr (M.-L. Giorgi)

Abstract

An Fe-Mn (1 wt. %) alloy was annealed at 800°C in N_2-5 vol. % H_2 with a dew point of -40°C. The nucleation and growth of external selective oxides of MnO were characterized ~~for the first time~~ as a function of ferrite grain orientation. Nucleation occurs successively on Fe{110}, Fe{111} and Fe{100} at 650 to 700°C. The oxides are faceted and their shape, size and surface density, measured accurately, are strongly dependent on the ferrite grain orientation. The oxides grow as the annealing time increases. New oxides are formed after 180 s at 800°C. The associated external selective oxidation mechanisms are discussed.

Keywords: A. alloy, B. AFM, B. SEM, B. STEM, C. selective oxidation.

1. Introduction

The steel sheets used for automotive vehicles are becoming thinner and thinner to achieve both lightweight of car bodies and reduced material costs. Advanced high strength steels (AHSS) are widely used in the automotive industry because they combine light weight with excellent mechanical properties [1]. The steel surface needs to be coated with a zinc layer in order to protect it against corrosion, which is usually done by hot-dip galvanizing [2]. Before being immersed in a bath of molten zinc or zinc alloy, the steel sheets are annealed in a reducing atmosphere of nitrogen and hydrogen (5 to 15 vol. %) containing only traces of water (about 200 ppm). The main objective of the annealing treatment is to recrystallize the steel and restore mechanical properties after cold rolling. Under the conditions chosen for the annealing treatment, the iron oxides formed during cold rolling are reduced, but unfortunately, selective oxidation occurs on the steel surface when it contains alloying elements such as manganese and silicon [2-5]. The presence of oxide

particles on the steel surface can lead to wettability problems by liquid zinc [1,2,6,7] and the coating quality is therefore directly related to the surface coverage by the oxide particles.

Numerous annealing studies have been made on AHSS to investigate the effect of steel composition, annealing temperature and dew point of the gas atmosphere on selective oxidation, including both laboratory materials [8-13] and industrial steels [5,12,14-19].

In general, oxidation is exclusively external during annealing in a low dew point atmosphere (≤ -30 °C). The segregation of Mn, Si and Al to the surface is dominant [5,8,10,12-14,16]. The simple oxides MnO, SiO_2, Cr_2O_3 and Al_2O_3 precipitate on the surface of the corresponding binary alloys and the formation of $MnSiO_3$ / Mn_2SiO_4 and $MnCr_2O_4$ occurs when Mn, Si and Cr are simultaneously present in the alloy [5,8,10,11,17]. With a long annealing time, the surface oxides can be connected to form a thin film of amorphous *a*-xMnO·SiO_2 ($x < 0.9$) and crystallized *c*-xMnO·SiO_2 ($x > 1$) [16,18,19].

Annealing in a high dew point atmosphere (≥ 0 °C) always results in the formation of small particles or thin films of external and internal oxides [10,12,13,15-19]. Larger simple oxide particles such as MnO, Mn_3O_4, SiO_2 and Cr_2O_3 are formed on and below the surface of the corresponding binary alloys and mixed oxides like $MnSiO_3$ / Mn_2SiO_4, $MnAl_2O_4$, $Mn_3(PO_4)_2$ and $MnCr_2O_4$ appear in the multi-constituent alloys [10,12,16-19].

These investigations have revealed that the selective oxidation behavior is very complex and that the chemical nature, morphology and distribution of oxides depend mainly on the steel composition and the annealing atmosphere. To reduce the formation of these oxide particles during annealing, it is important to understand the mechanisms of oxide nucleation and growth. Some authors have found that the segregation of the alloying elements on the steel surface [3], the size distribution, density [5,9,17,20] and shape [9,20] of the oxides are different from one ferrite grain to another or have shown crystallographic relationships between the oxide and the iron matrix [19]. The nucleation of these selective oxides must therefore be very sensitive to the characteristics of the steel surface (e.g. small defects, facets and grain orientation). It should be noted that some studies on the oxidation of iron (to iron oxides) as a function of ferrite grain orientation can be found ([21] and references inside). But, to our knowledge, no detailed studies have been carried out on the influence of ferrite grain orientation on the nucleation and growth of selective oxide particles formed during continuous annealing. The present study will therefore focus on this subject.

Due to the diversity and complexity of oxidation behavior, we focus on the selective oxidation of model systems consisting only of iron and manganese, Mn being one of the main alloying elements (typically 1.0 to 2.5 wt. % Mn) in AHSS. Recent studies on binary Fe-Mn alloys [8,9,11,20,22-25] have shown that only MnO particles are formed on the alloy surface under conventional industrial annealing conditions. The main objectives of this work are as follows: (1) to examine the first stage of selective oxide formation on the ferrite surface; (2) to characterize the two and three-dimensional geometrical parameters of the oxide

particles during annealing to study oxide growth; (3) to explore for the first time the influence of ferrite grain orientation on the nucleation and growth of the selective oxide particles.

2. Experimental procedure

2.1 Sample preparation

The binary Fe-Mn (1 wt. %) alloy used in this work was supplied by *Goodfellow* in the form of 1 mm thick sheet. The composition analyzed by Spark-Optical Emission Spectrometry (Spark-OES Spectrolab M10) is given in Table 1.

Table 1 Composition of the Fe-Mn alloy studied (wt. %).

C	Si	Mn	P	S	N	Cu	Ni	Fe
0.0013	0.002	1.043	0.002	0.001	0.0028	0.001	0.002	Bal.

The cold-rolled alloy sheets received were cut into 20 mm square samples for annealing experiments. In order to obtain a fully recrystallized microstructure, these square samples were first annealed at 950 °C for 60 min in a tubular resistance furnace (*ETR 1200*). The furnace gas atmosphere was composed of high-purity commercial nitrogen or helium (*Air Liquide*, less than 3 ppm H_2O, 2 ppm O_2 and 0.5 ppm C_nH_m) and was introduced at a flowrate of 3×10^{-5} $m^3 \cdot s^{-1}$ at standard temperature and pressure conditions (0 °C; 100 kPa). At the end of the annealing, the samples were cooled to room temperature at a rate of less than 1 $°C \cdot s^{-1}$ in the furnace chamber. The recrystallized samples were then mechanically polished with SiC papers to remove the iron oxides layer and mirror-polished up to 1 µm diamond suspension, resulting in an average roughness of a few nanometers. The obtained samples were ultrasonically cleaned in a pure ethanol solution and completely dried. Finally, two thermocouples were spot welded in the centre and in one corner of the samples to control and measure temperature for the subsequent annealing.

After this initial preparation, the samples were annealed in the quartz chamber of an infrared radiation furnace (*Ulvac Sinku-Riko* parabolic tubular furnace) with a temperature profile corresponding to continuous industrial annealing (thick line shown in Fig. 1). This annealing which lasts a few minutes will be called *short annealing* afterwards (to differentiate it from the first annealing which lasts 60 min). Two samples were first heated to 800 °C at a rate of about 6 $°C \cdot s^{-1}$ and then held at 800 °C for 60 s before being cooled to room temperature. To study the nucleation and growth of oxide particles, heating was stopped at various temperatures, namely 650, 680, 700, 730, 750, 770 and 800 °C, and the samples were cooled directly to room temperature (temperature profiles 1 to 7 in Fig. 1). In addition, some samples were annealed at 800 °C for 30,

120, 180, 240 and 300 s before being cooled to room temperature (temperature profiles 8 and 10-13 in Fig. 1). During annealing, the two temperature profiles obtained by the thermocouples were in good agreement. According to the Fe-Mn phase diagram [26], the samples were composed at all temperatures of ferrite, which has a body-centered cubic (*bcc*) structure with manganese in solid solution [27].

The gas atmosphere used in the furnace chamber was a high purity commercial N_2 - 5 vol. % H_2 mixture (*Air Liquide* with less than 3 ppm H_2O and 2 ppm O_2). It was introduced at a flowrate of 1.25×10^{-5} $m^3 \cdot s^{-1}$ at standard temperature and pressure conditions (0 °C; 100 kPa). The atmosphere dew point was set at -40 ± 2 °C, comparable to the practice of galvanizing lines and corresponding to an oxygen partial pressure of 5.8×10^{-19} Pa at 800 °C [28]. The dew point in the furnace chamber was measured by two aluminium oxide moisture probes located at the gas inlet and outlet, respectively. Due to the low temperature environment in the furnace chamber, cooling at the end of annealing is so rapid (about 4.5 °C·s^{-1} down to 650 °C) that it acts as a quench for selective oxidation reactions.

2.2 Characterization procedures

Under the annealing conditions described above, iron oxides are reduced and manganese is oxidized and forms particles on the alloy surface.

The surface of the samples was observed using a Field Emission Gun Scanning Electron Microscope (FEG-SEM *Leo 1530*). The orientation of the ferrite grains was determined by Electron Back Scattered Diffraction (EBSD *Nordif/TSL*). In order to be able to identify precise areas, two square marks with a size of 30 µm × 30 µm × 7 µm were made on each sample by the ion beam of a Focused Ion Beam Scanning Electron Microscope (Dual beam FIB-SEM *Helios FEI NanoLab 660*). Then, an area was selected around the mark to make an EBSD map and to determine the location of the ferrite grains with three orientations of {100}, {110} and {111}. For each annealing temperature, SEM photos were taken in three or four ferrite grains with the same orientation on one or two samples.

An image analysis using the *ImageJ* software [29,30] was performed on these SEM photos to obtain the geometrical parameters of the oxide particles. Since the oxides on the ferrite were low in contrast, we first drew the contours of the oxide particles by hand on a transparent film and scanned it to obtain an image, which allows automatic recognition of the oxide particles. Three geometrical parameters were measured: the surface density n_{oxides} of the oxides (i.e., the number of oxide particles present on a unit area), the surface area fraction covered by particles A_f and the equivalent diameter D_{eq} (diameter of the disc with the same surface as the particle S, i.e. $D_{eq} = \sqrt{4S/\pi}$). 6-8 SEM images were analysed for each orientation of ferrite grains annealed at the same temperature. The mean value and standard deviation of all these measurements were plotted on the graphs.

The samples were also observed by an Atomic Force Microscope (AFM *Bruker Nanoscope 5.0*) to obtain the geometry of the oxides in three dimensions. The AFM images were taken using the tapping mode with

PtSi-FM-20 tips (*Multimode 8.0 Bruker*) on several grains with the same grain orientation (2 to 4) of one or two samples which underwent the same annealing treatment. 3-4 AFM images were then processed with the *NanoScopeAnalysis* software. By defining the appropriate range of particle diameter, height and surface area, the oxide particles on the alloy surface were automatically recognized and the maximum height *H* of each particle (from the arithmetical mean of the heights over the entire surface analysed (9 or 25 μm^2) to the highest point of the oxide particle) was measured by the software. Since the oxides are partly below the ferrite surface, the height measured by this protocol underestimates the particle height, but nevertheless allows comparison of the maximum oxide heights for Fe{100} and Fe{111}. However, the particles on Fe{110} are completely below the ferrite surface and the oxides cannot be detected with the same protocol. In this case, a line has been drawn with the *NanoScopeAnalysis* software that cuts the particles. The height profile thus obtained makes it possible to measure the height *H* between the lower and the upper surface of each oxide. The mean value and standard deviation of the maximum heights for all measured images were plotted on the graphs.

The FIB-SEM microscope was used to prepare thin TEM samples in ferrite grains of different orientations. One TEM sample was prepared using FIB in Fe{100}, Fe{110} and Fe{111} grains annealed at 700 °C during heating and at 800 °C for 60 and 120 s during isothermal holding to observe the nucleation and oxide shape. TEM samples were also prepared using FIB in Fe{110} grains annealed at 800 °C during heating and for 300 s during holding, and in Fe{111} grains annealed at 800 °C for 180 s to observe the internal oxidation. Prior to extraction, a 2 µm Pt protective layer was deposited on the sample surface of the target milling area to prevent damage during the sample preparation. The size of the TEM samples was 15 µm × 5 µm and their thickness was 80-100 nm. The TEM samples were then observed using a Probe Cs Corrected Scanning / Transmission Electron Microscope (TEM/STEM-FEI *Titan3 G2 60-300*). The oxides' composition was analysed by Energy Dispersive Spectroscopy (4-detector Super-X EDS) in the STEM mode. The EDS spectra were processed quantitatively with the ESPRIT (Brucker) software using the Cliff-Lorimer method, which is suitable for quantitative analysis on thin samples.

3. Results

Theoretical calculations [8,20,31] and experimental works [9,11,20,21-25] have demonstrated that selective external oxidation occurs and that the oxide particles formed on the alloy surface are composed of MnO under the annealing conditions used in this work. The nucleation (section 3.1) and growth (section 3.2) of the oxide particles on the alloy surface during annealing will be described below.

3.1 Oxide nucleation

3.1.1 Recrystallization of the ferrite surface

Before the short annealing, all samples were annealed at 950 °C for 60 min to obtain a fully recrystallized microstructure. The subsequent mechanical polishing introduces new defects and stresses on the alloy surface. The restructuration of the damaged ferrite surface occurs during the heating stage of the short annealing.

Fig. 2 shows the EBSD maps obtained on samples annealed at 680 and 700 °C during heating and at 800 °C for 60 s during isothermal holding without any further surface preparation. The ferrite surface was not completely recrystallized at 680 °C (many points not measured by EBSD). The ferrite grains are clearly visible from 700 °C, which means that the ferrite surface is well recrystallized.

The ferrite grain size does not change during short annealing (Fig. 2). The mean value of the equivalent diameter of the ferrite grains is constant and equal to 73 ± 39 µm. This measurement was compared to the ferrite grain size before short annealing, measured on EBSD maps (not shown here). These EBSD cards were made on a mechanical- and mirror- polished sample (details in section 2.1) and then polished by vibration with a SiO_2 suspension for 5 h to remove the damaged surface. The ferrite is well recrystallized after the initial long annealing and the equivalent grain diameter is 83 ± 44 µm. This diameter is similar to the diameter measured on the short-annealed samples, where only the extreme surface restructures.

3.1.2 Oxide nucleation temperature range

The oxide particles appear at 650 °C, mainly within the grain boundaries (indicated by the white arrows in Fig. 3(a)). Oxides could not be observed at this temperature in the grains using SEM and AFM. The oxide nucleation is therefore favoured at the grain boundaries, which are diffusion short-circuits. As the sample surface is not yet completely recrystallized (Fig. 2(a)), many defects or sub-grain boundaries and polishing lines are observed, which are preferential locations for nucleation. Defects in the ferrite surface and subsurface probably promote nucleation of oxide particles. The interaction between recrystallization and selective oxidation has not been further investigated here.

Nucleation of very small oxide particles starts at 680 °C on some ferrite grains only (Fig. 3(b)). This result shows that nucleation does not occur simultaneously on all grains and depends on the orientation of the ferrite grains on which they are formed. Their equivalent diameter is 21 ± 6 nm. The starting temperature of nucleation in the ferrite grains, between 650 and 680 °C, cannot be determined more precisely due to the resolution limit of the devices used.

The oxide particles are visible on all grains by SEM at 700 °C (section 3.1.3). Under the operating conditions used here, the oxide nucleation occurs first at the grain boundaries and then in the grains between 650 and 700 °C. Using Becker-Döring nucleation theory [32,33], the critical radius of the MnO nuclei formed under our annealing conditions was estimated to be less than 1 nm [24]. Such small nuclei are not

visible at SEM and probably not at AFM at low temperature due to defects on the ferrite surface. The nucleation temperature range may be overestimated.

In the following, we will focus on the effect of ferrite grain orientation on the nucleation and growth of the oxides. Three typical grain orientations have been chosen, namely Fe{100}, Fe{110} and Fe{111}.

3.1.3 Influence of ferrite grain orientation on oxide nucleation

The small size of the oxides formed and the surface defects of ferrite due to mechanical polishing do not allow good quality SEM and AFM images to be obtained at annealing temperatures below 680 °C (sections 3.1.1 and 3.1.2). The annealing temperature considered for the study of the influence of ferrite grain orientation on oxide nucleation will therefore be 700 °C.

Numerous round or elongated black spots a few tens of nanometers in size are present on Fe{100} and Fe{110} at an annealing temperature of 700 °C (Figs. 4(a) and (b)). Very small white spots a few tens of nanometers in size appear on Fe{111} (Fig. 4(c)).

AFM was used to accurately measure the particle equivalent diameter on Fe{100}, Fe{110} and Fe{111} of samples annealed at 700 °C (Fig. 5). White spots with a diameter of 35 ± 11 nm can be observed on Fe{100} (Fig. 5(a)). The particles present on Fe{111} have a mean equivalent diameter of 60 ± 18 nm (Fig. 5(c)) and the largest particles are observed on Fe{110} with an equivalent diameter of 88 ± 13 nm (Fig. 5(b)). All particles are larger than the nascent nuclei (size less than 1 nm [24, 32,33]), which means that they have already grown for some time. It can therefore be concluded that particles are present on the surface of all alloy grains after annealing at 700 °C and that nucleation occurs at a temperature below 700 °C, first on Fe{110} and then on Fe{111} and Fe{100} (assuming that the particle size is mainly dependent on growth time, regardless of the orientation of the ferrite grain). The maximum height difference between the oxide particles and the ferrite substrate is 13, 15 and 68 nm on Fe{100}, Fe{110} and Fe{111} respectively. The higher oxides relative to the alloy surface give a local electron charging effect so that the oxide particles on Fe{111} appear white on the SEM images (Fig. 4).

To determine the chemical nature of the oxide particles formed at 700 °C, a quantitative STEM / EDX analysis was performed on the FIB prepared samples in Fe{100}, Fe{110} and Fe{111}. The EDX maps of O in red, Mn in green and Fe in blue are shown with their superposition for the three orientations (Fig. 6).

A round particle with a diameter of 20 nm is partially embedded in the surface of Fe{100} (Fig. 6(a)). Its quantitative composition is 47.6 at. % Mn, 45.0 at. % O and 7.4 at. % Fe. Mn and O are present in the same atomic proportion. A flat particle about 220 nm long can be observed on Fe{110} (Fig. 6(b)) and two round particles about 65 nm long on Fe {111} (Fig. 6(c)). Quantitative analysis shows that all these particles (4 to 6 particles per orientation) contain mainly Mn and O in the same atomic proportions and iron in a smaller proportion (from 10 to 25 at. %). These cross-section observations also show that the oxidation is external.

All three grains are covered with a layer of native iron oxides (which forms after annealing when the sample is brought into contact with air).

According to the EDX analysis, the particles can be composed of MnO or a MnO-FeO solution. However, as the thickness of the TEM sample is about 100 nm, which is larger than the size of the oxide particles, the low Fe content is probably due to the contribution of the underlying ferrite. The oxides are therefore probably be composed of MnO only. This is consistent with the thermodynamic calculations (section 4.1). To confirm this, the oxides should be extracted on a C replica to perform the analysis without the possible artefact due to the presence of the substrate.

3.2 Oxide growth

The growth of oxide particles on Fe{100}, Fe{110} and Fe{111} was studied for annealing at 750, 770, 800 °C during heating and at 800 °C for 30, 60, 120, 180, 240 and 300 s during isothermal holding. The chemical composition of the oxide particles is given in section 3.2.1. The main geometrical parameters obtained are described in section 3.2.2. Particular emphasis is placed on the second growth which occurs after 180 s at 800 °C in section 3.2.3.

3.2.1 Chemical composition

STEM/EDX analyses of O in red, Mn in green and Fe in blue are presented with their superposition for the three orientations, after annealing at 800 °C for 60 s (Fig. 7) and 120 s (Fig. 8). In all cases, oxide particles are mainly formed on the surface of the annealed samples (external oxides). Smaller oxides are also occasionally present below the surface (internal oxides).

The external particles are rich in Mn and O. Quantitative analysis shows that Mn and O are present in the same atomic proportions in most external oxides (36 out of 43), meaning that they are MnO oxides. Fe is also detected in these oxides, probably due to the contribution of the underlying ferrite grain. For some external oxides (7 out of 43), the atomic ratio of Mn and O is about 3:2. However, Mn_3O_2 is not a thermodynamically stable phase [34-37] and should not exist under our conditions. The most likely hypothesis is that there is a small excess of Mn in ferrite at these locations.

O, Mn and Fe (at more than 70 at. %) are detected in internal oxides by EDX analyses. The presence of Fe is mainly due to the contribution of ferrite. These internal oxides are formed occasionally and their composition, shape and quantity are not dependent on ferrite grain orientation. During long-term annealing at 800 °C, oxygen atoms penetrate into the alloy and cause a slight internal oxidation of Mn. However, the amount of internal oxides is very low. Under the annealing conditions studied in this work, the selective oxidation of Mn is mainly external.

3.2.2 Geometrical parameters of oxide particles

All samples were observed by SEM to determine the surface density n_{oxides}, the equivalent diameter D_{eq} and the surface coverage fraction A_f of the oxides as a function of ferrite grain orientation and annealing time (3.2.2.1). The three-dimensional shape of the oxide particles and their mean maximum height H were determined using AFM (3.2.2.2). These geometrical parameters are summarized in Fig. 10 and the detailed data are presented in Supplementary Material A.

3.2.2.1 Geometrical parameters of oxides

The Fe-Mn alloy surfaces were first observed by SEM after annealing at 750 and 800 °C during heating and at 800 °C for 60, 120, 180, 240 and 300 s during isothermal holding (Fig. 9). The ferrite surfaces present facetted steps at all temperatures and oxides are formed on these facetted steps. On samples annealed at 750 °C (Fig. 9(a-c)), the oxides are facetted crystals whose shape depends on the ferrite grain orientation: cubes or square pyramids on Fe{100}, assemblies of triangular prisms or pyramids on Fe{110} and polygonal prisms or pyramids on Fe{111}. When annealing continues, the oxide particles on Fe{100} remain as larger and larger cubes or square pyramids (first column in Fig. 9). The oxide particles on Fe{110} change from single to multiple overlapping triangular prisms or pyramids and then to very elongated particles probably polycrystalline (middle column in Fig. 9). The oxide particles on Fe{111} remain polygonal prisms or pyramids and increase in size. For holding time at 800 °C of 180 s (Fig. 9(m-o)), 240 (Fig. 9(p-r)) and 300 s (Fig. 9(s-u)), very small oxide particles appear between the large particles on all three ferrite grain orientations.

The characteristic geometrical parameters of the oxides obtained by image analysis are plotted as a function of the annealing step (temperature-time) for the three ferrite grain orientations in Fig. 10. The surface density of oxides n_{oxides} is the highest and the mean equivalent diameter D_{eq} is the lowest on Fe{100}. The lowest n_{oxides} and the largest D_{eq} are obtained on Fe{110}, and these parameters are intermediate on Fe{111}. The surface area fraction covered by oxides A_f is in the following increasing order: Fe{111} < Fe{100} < Fe{110}. As the annealing temperature or the annealing time increases, the surface area fraction covered by oxides on the three grain orientations increases (Fig. 10(c)). For a holding time of less than 120 s, n_{oxides} remains almost constant (Fig. 10(a)) and D_{eq} increases (Fig. 10(b)) for the three grain orientations. For a holding time longer than 120 s, n_{oxides} increases and D_{eq} decreases. The reason for this sudden change in oxidation behaviour is due to the growth of new small crystals (section 3.2.3). In order to highlight the formation of small crystals at the end of annealing, the distribution profiles of D_{eq} during growth are given in Supplementary Material B.

3.2.2.2 Three-dimensional shape of oxides

The three-dimensional shapes of the oxide particles were measured by AFM for Fe{100}, Fe{110} and Fe{111} under all annealing conditions (Fig. 11). The complexity of the oxides' shape is highlighted by the

colour contrast, corresponding to the height scale. To obtain a clearer idea of the shape, the height of some oxide particles has been plotted according to their lateral dimension using the same scale on the abscissa and ordinate (Fig. 12). The selected oxides are marked by red, green and blue lines on Fe{100}, Fe{110} and Fe{111} respectively in Fig. 11. For each orientation and holding time at 800 °C, the selected oxides are representative of the population of oxides present.

On Fe{100} (left column), the oxide particles have the smallest lateral dimension and appear as cuboids slightly raised above the alloy surface. On Fe{110} (middle column), the oxide particles are flat cuboids of very large lateral dimension, with the upper surface remaining more or less at the same height as the sample surface. On Fe{111}, the oxide particles are above the alloy surface. They have a shape of polygonal pyramids, the maximum height of which is about a quarter of the lateral dimension.

As oxides can grow below the alloy surface, we also observed oxide particle cross-sections by STEM (Fig. 13). The oxides in side view are diamond-shape on Fe{100} and Fe{111}. They lie within the facets formed on the ferrite surface. On Fe{110}, the oxides in side view appear as elongated parallelograms, which are contained in depressions in the alloy surface and the ferrite / oxide interface remains flat.

The maximum height H of each oxide, determined by AFM, is the distance between the highest point of the oxide and the arithmetical mean of the heights over the entire surface analysed (5×5 or 3×3 μm^2) for Fe{100} and Fe{111} and the distance between the lower and upper surfaces of the oxide on Fe{110} (section 2.2). The mean maximum height H is plotted as a function of annealing temperature and time for each ferrite grain orientation in Fig. 10(d). The maximum oxide height is also measured on the FIB cross-sections of the samples using STEM images (H', Fig. 13). H' is plotted in Fig. 10(d) with diamonds for comparison with H measured by AFM. H' is always higher than H, probably due to the uncertainty of the AFM calculation which consists in using the arithmetical mean of the heights over a large surface area. H' is a more local measurement. For oxides on Fe{110}, both H and H' measure the distance between the lower and the upper surfaces of the oxide. However, the oxides are very thin and their thickness can be overestimated when measured with STEM images. In conclusion, AFM and STEM give the same trends on the influence of ferrite grain orientation on oxide height. For the STEM, the number of observed oxides is too low to obtain a mean oxide height and an uncertainty on this height. For this reason, AFM is preferred for our study because this technique allows a more statistical analysis of oxide heights.

The mean maximum oxide height increases during heating and during holding at 800 °C for up to 120 s and then decreases with the growth of the small particles mentioned above (Fig. 10(d)). This second growth is detected earlier by AFM (120 s instead of 180 s) because this technique has a better resolution than SEM. The mean maximum oxide height is always greater and increases more rapidly on Fe{111} than on the other two orientations.

In conclusion, the oxides on Fe{110} preferentially grow laterally and the oxides on Fe{100} and Fe{111} grow in both horizontal and vertical directions. Many small particles are visible on the surface of the samples annealed at 800 °C for 120 to 300 s (Fig. 11). The second growth phase will be discussed in the next section.

3.2.3 Second growth

The mean equivalent diameter of the oxides shows a sudden decrease and their surface density a sudden increase when the samples are annealed at 800 °C for 180 s (Figs. 10(a) and (b)), which is due to the growth of new crystals. To better understand the growth mechanisms at 800 °C, the annealed samples were observed using SEM at a lower magnification than in Fig. 11 (Fig. 14). The corresponding small particle size distribution profiles are summarized in Supplementary Material C.

Numerous white spots a few nanometers in size are present on Fe{100}, Fe{110} and Fe{111} after annealing at 800 °C for 180 s (Figs. 14(m-o)). They were not visible for shorter annealing time (Figs. 14(a-l)) and 9(d-l)). After annealing at 800 °C for 240 and 300 s, many small particles are present on the samples (Figs. 14(p-u)), which is probably due to the growth of these white spots. The presence of the new very small particles leads to an increase in surface density and a decrease in the mean equivalent diameter of the oxide particles (Figs. 10 (a) and (b)). This analysis is confirmed by the particle size distributions (Supplementary Material C) which show that the relative frequency of very small particles (0-20 nm for Fe(100), 0-50 nm for Fe{110} and Fe{111}) first decreases (from 0 to 180 s), then increases when the samples are annealed at 800 °C for 180 to 300 s.

For samples annealed at 800 °C for 0 to 120 s, there are also very small particles present on the surface, especially on Fe{110} (Fig. 14). The influence of these small particles is negligible on the overall growth behaviour of big particles (Fig. 10).

In summary, the selective external oxidation of Fe-Mn (1 wt. %) alloys annealed at 800 °C in N_2-H_2 (5 vol. %) with a dew point of -40 °C can be divided into three main steps: (i) nucleation of the oxide particles; (ii) growth of some nuclei and coalescence into larger particles when the oxides meet (mainly on Fe{110}) and (iii) second growth of other nuclei. These different growth stages and the associated external selective oxidation mechanisms will be discussed in section 4.

4. Discussion

4.1 Thermodynamic stability of iron and manganese oxides

The possible reactions between iron (Fe) and its oxides (Fe_xO_z) in the annealing atmosphere of N_2 – 5 vol. % H_2 are given by:

$$x\,Fe(s) + z\,H_2O(g) \leftrightarrow Fe_xO_z(s) + z\,H_2(g) \qquad \text{(R-1)}$$

The Gibbs free energy associated with the reaction (R-1) at constant temperature and pressure can be expressed as [38]:

$$\Delta_r G_{R-1} = \Delta_r G^{\circ}_{R-1} + RT \ln\left(\frac{a_{Fe_xO_z}}{a_{Fe}^{x}} \frac{{P_{H_2}}^{z}}{{P_{H_2O}}^{z}}\right) \quad \text{Eq. (1)}$$

where $\Delta_r G^{\circ}_{R-1}$ is the standard Gibbs free energy of reaction (R-1), $a_{Fe_xO_z}$ and a_{Fe} are the activities of Fe_xO_z and Fe, P_{H_2} and P_{H_2O} are the partial pressures of H_2 and H_2O, R is the ideal gas constant (8.314 J·mol^{-1}·K^{-1}) and T is the temperature. As a first approximation, the oxides formed can be considered pure, i.e., $a_{Fe_xO_z} = 1$. As Fe is the main element of the Fe-Mn alloy under study (99.00 wt. %), its activity is assumed to be given by Raoult's law:

$$a_{Fe} = x_{Fe} \approx 1 \quad \text{Eq. (2)}$$

The value of $\Delta_r G^{\circ}_{R-1}$ can be taken from FactSage 7.2 (http://www.factsage.com/). The hydrogen partial pressure used in this work is 5066 Pa. The partial pressure of water corresponding to a dew point of -40 °C is 19 Pa [39].

With all the equations and values given above, the thermodynamic stability of iron oxides, i.e. $Fe_{0.95}O$, Fe_2O_3 and Fe_3O_4 can be determined as a function of annealing temperature. The Gibbs free energy of the reaction (R-1) is greater than zero for all iron oxides when the temperature is above than 175 °C. The native iron oxides are therefore completely reduced under the annealing conditions used in this work and the metallic iron is stable for temperatures above 175 °C.

In a second step, we compare the stability of the different Mn oxides (Mn_2O_3, Mn_3O_4, MnO and MnO_2) under the annealing conditions used here. The Gibbs free energy $\Delta_r G_{R-2}$ for the transformation of MnO into the other oxides (R-2) can be calculated as follows:

$$\mathrm{MnO(s)} + \frac{\mathrm{z-x}}{\mathrm{2x}}\mathrm{O_2(g)} = \frac{1}{\mathrm{x}}\mathrm{Mn_xO_z(s)} \quad \text{(R-2)}$$

$$\Delta_r G_{R-2} = \Delta_r G^{\circ}_{R-2} + RT \ln \frac{\left(a_{Mn_xO_z}\right)^{1/x}}{a_{MnO} \cdot \left(P_{O_2}\right)^{(z-x)/2x}} \quad \text{Eq. (3)}$$

Assuming that MnO and Mn_xO_z are pure, their activities are equal to 1. The oxygen partial pressure in atm (Eqs. 3 and 4) is related to the partial pressure of water vapor and temperature [28]:

$$\log P_{O_2} = 6 - \frac{26176}{T} + 2\log\left(\frac{P_{H_2O}}{P_{H_2}}\right) \quad \text{Eq. (4)}$$

Using Eqs. (3) and (4), it is found that the value of $\Delta_r G_{R-2}$ is always well above zero when the temperature rises from 20 to 800 °C, which means that MnO is the most stable Mn oxide under the annealing conditions studied in this work.

In conclusion, the iron oxides are reduced and Mn is oxidized to MnO under the annealing conditions used in this work.

4.2 Mechanisms of Mn selective oxidation

4.2.1 Oxidation mechanisms of manganese

When the Fe-Mn alloy is brought into contact with the annealing atmosphere, water vapour is adsorbed and dissociated on the alloy surface as follows [40-44]:

$$H_2O(g) \rightarrow H_2O(ad) \rightarrow OH(ad) + H(ad) \rightarrow O(ad) + H_2(g) \rightarrow O(dis) \quad \text{(R-3)}$$

In the last step of the reaction scheme (R-3), the adsorbed oxygen atom dissolves in the ferrite surface. The O weight fraction dissolved in ferrite in equilibrium with N_2 - 5 vol. % H_2 at the dew point of -40 °C is calculated in ppm with [28]:

$$\log w_O^{equi} = 4 - \frac{3690}{T} + \log\left(\frac{P_{H_2O}}{P_{H_2}}\right) \quad \text{Eq. (5)}$$

MnO oxides precipitate if:

$$w_{Mn} \cdot w_O \geq K_{MnO} \quad \text{Eq. (6)}$$

with the solubility product of MnO expressed in ppm^2 given by Huin *et al.* [28]:

$$\log K_{MnO} = 10.95 - \frac{10830}{T} \quad \text{Eq. (7)}$$

The nucleation of MnO particles occurs between 650 and 700 °C according to our observations (section 3.1.2). Assuming that the Fe-Mn alloy is in equilibrium with the gas atmosphere at 650°C, the O weight fraction dissolved in the alloy at its surface is 0.0038 ppm (Eq. (5)). The corresponding weight fraction of Mn required for the formation of MnO is 44 ppm, namely 0.0044 wt. % (Eq. (7)). Consequently, the alloy, which contains 1 wt. % Mn, is supersaturated at its surface with dissolved oxygen and manganese. This supersaturation leads to the nucleation / growth of MnO at the alloy surface. The solid diffusion of Mn towards the alloy surface then allows the growth of MnO particles.

4.2.2 Selective external oxidation

The operating conditions of the annealing process cause Mn selective oxidation (section 4.2.1). This selective oxidation can be internal or external. Wagner proposed a robust model for the selective oxidation of binary alloys in a low oxygen atmosphere [45,46]. Using Wagner's model, one can calculate the critical Mn mole fraction for the transition from internal to external oxidation:

$$x_{Mn}^{crit} = \left(\frac{\pi \cdot g^* \cdot x_O^{surf} \cdot D_O \cdot V_{alloy}}{2 \cdot D_{Mn} \cdot V_{MnO}}\right)^{0.5} \quad \text{Eq. (8)}$$

where g^* is the critical volume fraction of the internal oxide equal to 0.3 [47,48], x_O^{surf} is the oxygen mole fraction at the alloy surface related to w_O^{equi} (1.4×10^{-6} wt. % at 800 °C), D_O and D_{Mn} are the diffusion coefficients of Mn and O in ferrite (8.02×10^{-12} and 9.09×10^{-16} $m^2 \cdot s^{-1}$ at 800 °C [28]), and V_{alloy} and V_{MnO} are the molar volumes of the binary alloy and MnO respectively (7.22×10^{-6} and 1.33×10^{-5} $m^3 \cdot mol^{-1}$ [49]). For annealing at 800 °C, x_{Mn}^{crit} is evaluated at 0.01, which is equal to the composition of the binary alloy studied here. The selective oxidation of Mn must therefore be mainly external according to this calculation. Our experiments have confirmed this (Figs. 7 and 8).

Although the selective oxidation of MnO is mainly external, the inward diffusion of oxygen cannot be completely stopped and some very small manganese oxides may form below the alloy surface during an annealing time of more than 60 s (Fig. 7).

4.3 Influence of ferrite grain orientation

4.3.1 Ferrite surface facets

For a solid crystal, the surface energy depends on the crystallographic plane considered. A macroscopically flat surface is unstable if the total surface energy decreases when a hill-and-valley structure, consisting of macroscopic surfaces of different orientations, is formed [50]. As the annealing temperature rises, the alloy surface becomes highly facetted with numerous steps visible from 700 °C (Figs. 4 and 5). This means that the crystallographic planes Fe{100}, Fe{110} and Fe{111} are not stable at high temperature in N_2 - 5 vol. % H_2 with a dew point of -40 °C.

We found no published studies dealing with faceting of the vicinal surfaces of Fe at high temperature. More generally, studies on body centered cubic systems are few and mainly concern Mo and W [51-53]. The adsorption of oxygen atoms can make a vicinal surface unstable and cause faceting [51-54]. In the system we are studying, in addition to oxygen adsorption, ~~MnO particles grow together with Fe~~ ~~facets~~ MnO particles form on facets and steps (Figs. 9(n) and (q)). The interaction between MnO and the Fe surface is thus very complex. Determining the orientations of the planes that delimit the facets requires specific experiments (e.g. using the TEM) and is beyond the scope of our study.

4.3.2 Nucleation of MnO particles

The MnO oxides clearly nucleate at the edges and kinks of the Fe steps (Figs. 4 and 5). The manganese atoms present there have a lower coordination than those on the terraces and constitute preferential nucleation sites for MnO [51]. Nucleation occurs on the steps when sufficient oxygen and manganese atoms are present in the same place by diffusion of adatoms along the steps.

Annealing experiments at 700 °C show that the oxide particles nucleate first on Fe{110}, then on Fe{111} and Fe{100} (section 3.1.3). MnO nucleation is favoured on Fe{110} because the surface energy between MnO and Fe{110} is probably lower than that between MnO and other ferrite grain orientations. These

surface energies are not known but can be compared using the DFT (Density Functional Theory) evaluation of the surface energy for Fe{100} and Fe{110} planes, respectively 2.29 and 2.27 J/m^2 [55]. Both are of the same order of magnitude. Since~~This can be inferred from the small contact angle andthe elongated shape of~~ the MnO particles on Fe{110} are more elongated than on Fe{100} (Figs. 6, 7, 8 and 13), it can be deduced that the surface energy between MnO and Fe{100} is higher than between MnO and Fe{110}. Based on the shape of the MnO particles, the same conclusion can be drawn for Fe{111}, although in this case the surface energy is slightly different, i.e. 2.5 J/m^2 [55]. Fe{110} is the ferrite grain orientation that is best wetted by MnO.

This is confirmed using Becker-Döring nucleation theory [32,33] to calculate the heterogeneous nucleation rate of MnO oxides:

$$I = N_S \beta^* Z \exp\left(\frac{-\Delta G^*}{k_B T}\right) \quad \text{Eq. (9)}$$

where N_S is the number of sites where an embryo can form per unit area, β^* the growth rate of a critical nucleus, Z the Zeldovich factor, ΔG^* the Gibbs free energy of formation of a spherical cap-shaped MnO embryo with critical radius r^*, k_B the Boltzmann constant and T the temperature. L. Gong *et al.* [24] gave a detailed description of the nucleation parameters of the MnO oxides on the Fe-Mn alloy surface. Z, β^* and ΔG^* are functions of the contact angle θ between MnO and ferrite. For the calculation of the nucleation rate, only N_S and θ depend on the orientation of the ferrite grains.

The ~~effective~~ apparent contact angle θ_{app} between the ferrite surface and the tangent to the particle at the triple line is measured from the cross-sections of the oxide particles (Fig. 13). The mean value of θ_{app} is 63° ± 15°, 14° ± 6° and 51° ± 9° for Fe{100}, Fe{110} and Fe{111} respectively. It is very important to be aware that the apparent contact angle is influenced by the anisotropic crystal shape in solid wetting and is not as simply described by the Young's equation as in liquid wetting [56]. Despite this remark, the apparent contact angle θ_{app} is taken for the contact angle θ of the assumed hemispherical nuclei in the calculation here.

N_S is equal to $\frac{x_{Mn}^{surf}}{a^2}$, $\frac{\sqrt{2}x_{Mn}^{surf}}{a^2}$ and $\frac{x_{Mn}^{surf}}{\sqrt{3}a^2}$ on Fe{100}, Fe{110} and Fe{111} respectively. x_{Mn}^{surf} is the molar fraction of Mn at the alloy surface (supposed to be equal to the molar fraction of Mn in the alloy ~1 mol. %) and a is the lattice parameter of ferrite (= 0.287 nm [57]). The nucleation rates of MnO oxides (Eq. (9)) on Fe{100}, Fe{110} and Fe{111} at 700 °C are 1.9×10^{9}, 1.5×10^{19} and 5.7×10^{13} m^{-2}·s^{-1} respectively. The nucleation rate is in the order Fe{110} > Fe{111} > Fe{100}, which is in good agreement with the experiments.

4.3.3 Growth and shape of MnO particles

As the annealing temperature increases, the oxides become larger and their shape depends on the underlying ferrite grain but does not appear to change much during growth (Fig. 9).

During the transformation of the system consisting of a particle of MnO resting on a particular orientation of Fe(*hkl*), an infinitesimal variation of the total Gibbs free energy is written:

$$dG = Vdp - SdT + \sum \mu_i dn_i + \sum \gamma_j dA_j \qquad \text{Eq. (10)}$$

where V, p, S and T are the volume, pressure, entropy and temperature of the system, μ_i and n_i are the chemical potential and the number of moles of i (i = Mn and O) in the system, γ_j and A_j are the surface energy and surface area of each side j of the faceted MnO particle. Strictly speaking, the calculation of dG must also take into account the deformation of the material and the surface and interface stresses [58], which are neglected in a first approximation [59]. In general, the crystal shape is studied at constant temperature, pressure and mole number so that the equilibrium crystal shape corresponds to the minimization of $\sum \gamma_j dA_j$ [56,59]. In our case, the annealing is non-isothermal and the number of moles increases as the particles are growing. Since the crystal shape does not change during the non-isothermal annealing, this means that the influence of temperature is negligible, especially on the variation of γ_j. MnO crystals are thought to reach their equilibrium crystal shape at temperatures above 700 °C, corresponding to the minimization of $\sum \gamma_j dA_j$ (probably the predominant term in dG). Growth, represented by the term $\sum \mu_i dn_i$, does not lead to a change in shape either.

For a faceted MnO particle, each facet is a crystallographic plane with a particular orientation. $\sum \gamma_j dA_j$ includes the surface and interface energy of all facets constituting the MnO particle: (i) the MnO surface energy for different crystallographic planes $\gamma_{MnO}(\overrightarrow{n_j})$ with $\overrightarrow{n_j}$ the normal to facet j, (ii) the MnO/Fe interfacial energy $\gamma_{MnO/Fe}(\overrightarrow{n_j})$ for different crystallographic planes since the particles rest in Fe kinks (Figs. 7 and 8) and (iii) the Fe surface energy $\gamma_{Fe}(\overrightarrow{n_j})$ which depends on the orientation of the ferrite grain at the triple line of the MnO particle.

If the MnO particle under consideration were equilibrated in the gas atmosphere, without contact with iron, it would reach its equilibrium crystal shape or Wulff shape composed of the most stable crystallographic planes, i.e. those with the lowest $\gamma_{MnO}(\overrightarrow{n_j})$ surface energy. When the MnO particle rests on iron, its Wulff shape is equilibrated on a solid substrate of a dissimilar material and the MnO/Fe(*hkl*) interfacial energies are involved (Winterbottom analysis described in Refs. [56,59]). The surface energy of iron crystallographic planes depends on their orientation (e.g., 2.29, 2.27 and 2.5 J/m^2 for Fe{100}, Fe{110} and Fe{111} [55]). Although the $\gamma_{MnO/Fe}(\overrightarrow{n_j})$ interfacial energies are not known, it is thought that they also depend on the Fe orientation. The orientation of the Wulff shape with respect to the iron plane will therefore probably depend on the Fe orientation, giving rise to the different apparent shapes of MnO oxides on Fe{100}, Fe{110} and Fe{111}.

The next step of this part of the study would be the determination of the crystal facet orientations, but this requires specific experiments (using TEM and EBSD [60-64]) and is beyond the scope of this study.

As already mentioned in the nucleation part (section 4.3.2), the interface energy between MnO and Fe{110} is lower than that between MnO and other ferrite grain orientations. This difference explains why MnO particles prefer to grow in both the horizontal and vertical directions on Fe{100} and Fe{111} and extend laterally on Fe{110}.

4.4 Very small particles

As indicated in section 3.2.3, the mean equivalent diameter of the oxides shows a sudden decrease and their surface density a sudden increase when the samples are annealed at 800 °C for 180 s (Figs. 10(a) and (b)). This has been attributed to the growth of new crystals, which are visible on the alloy surface between the large oxide particles (Fig. 14). We propose the following mechanism to explain this second growth.

When the annealing temperature rises to 700 °C, MnO nuclei are formed on the alloy surface. Only part of the nuclei grow with increasing temperature, perhaps because they are located in the vicinity of defects (dislocations, sub-grain boundaries, ferrite kinks or edges), which favour high diffusion of Mn [65]. These first oxide particles grow competitively [66]. The other part of the nuclei do not grow but remain present among the large ones.

Oxide growth requires that the manganese atoms diffuse from the alloy bulk to the surface and then diffuse through the oxide particles (if the oxidation front is on the outer surface of the oxides). As the particle size increases, the diffusion of manganese into the oxides takes more time. In addition, manganese becomes depleted around these oxide particles. These phenomena explain a slowing down of the large particles growth, which may facilitate the growth of the other nuclei present. The result is the presence of many very small particles that become visibly by means of the SEM on the alloy surface when annealed at 800 °C for more than 180 s. Further studies at the atomic level are needed to better understand this second growth.

5. Conclusions

The nucleation and growth of oxide particles on binary Fe-Mn (1 wt. %) alloys were studied during an annealing process representative of industrial continuous annealing (800 °C, N_2-H_2 (5 vol. %), -40 °C dew point). Complementary techniques were used to characterize the oxide particles on the alloy surface: EBSD maps were measured to determine the ferrite grain orientation; a scanning electron microscope and an atomic force microscope were used to determine the geometrical characteristics of the oxide particles and EDS analysis were performed on thin FIB foils to determine the chemical nature of particles.

Under the operating conditions studied, the Mn selective oxidation is mainly external, i.e. MnO particles are formed on the alloy surface. Oxides first appear at the grain and sub-grain boundaries on the samples annealed at 650 °C during heating. As the annealing temperature rises, the MnO oxides nucleate successively on Fe{110}, Fe{111} and Fe{100}. When annealed at 750 and 800 °C during heating and at 800 °C for 30 to

546 120 s during isothermal holding, the surface density of oxides remains constant and the mean equivalent
547 diameter and maximum height increase continuously. During this time, the oxides have different shapes from
548 one ferrite grain to another: cuboids slightly raised above the alloy surface on Fe{100}, flat cuboids of very
549 large lateral dimension embedded in the surface of Fe{110} and polygonal pyramids raised above the surface
550 on Fe{111}. When annealed at 800 °C for 180 s, the surface density of oxides suddenly increases and the
551 mean equivalent diameter decreases. Many very small particles are present on the alloy surface after
552 annealing at 800 °C for more than 180 s. More and more very small particles are formed with longer
553 annealing time. The surface area fraction covered by oxides increases continuously as the annealing time
554 increases.

555 The underlying ferrite grain orientations show a significant influence on the nucleation and growth of
556 MnO oxides. The oxides first nucleate on Fe{110} and have the largest mean equivalent diameter and the
557 smallest height. The oxides' surface density on Fe{100} is much higher and their mean equivalent diameter
558 is much smaller than those on Fe{110} and Fe{111}. The oxides on Fe{111} always have the greatest
559 height. The oxides extend laterally on Fe{110} and grow in both horizontal and vertical directions on
560 Fe{100} and Fe{111}.

561 Reaction mechanisms are proposed in the last part of this work.

562

563 **Acknowledgements**

564

565 This work was supported by the French "Agence Nationale de la Recherche" through the "Investissements
566 d'avenir" program (ANR-10-EQPX-37 MATMECA) and the China Scholarship Council (201604490035).
567 The authors are extremely grateful to Dominique Chatain and Jean-Michel Mataigne for fruitful discussions.

568

569 **Data availability**

570 The raw/processed data required to reproduce these findings cannot be shared at this time due to technical or
571 time limitations. They are available on request.

572

573

574 **References**

575 [1] G. Angeli, J. Faderl, 'Galvanized in Europe' -- An actual status and challenges for the future, in:
576 Galvatech 2015: 10th Int. Conf. on Zinc and Zinc Alloy Coated Steel Sheet, Association for Iron and Steel
577 Technology AIST, Toronto, 2015, pp. 19-27.

578 [2] A.R. Marder, The metallurgy of zinc-coated steel, Prog. Mater. Sci. 45 (2000) 191-271.
579 http://dx.doi.org/10.1016/S0079-6425(98)00006-1.

580 [3] H.J. Grabke, V. Leroy, H. Viefhaus, Segregation on the surface of steels in heat treatment and oxidation,
581 ISIJ Int. 35 (1995) 95-113. https://doi.org/10.2355/isijinternational.35.95.

582 [4] I. Cvijovic, I. Parezanovic, M. Spiegel, Influence of H_2-N_2 atmosphere composition and annealing
583 duration on the selective surface oxidation of low-carbon steels, Corros. Sci. 48 (2006) 980-993.
584 https://doi.org/10.1016/j.corsci.2005.02.022.

585 [5] A. Ollivier-Leduc, M.-L. Giorgi, D. Balloy, J.-B. Guillot, Nucleation and growth of selective oxide
586 particles on ferrite steel, Corros. Sci. 52 (2010) 2498-2504. https://doi.org/10.1016/j.corsci.2010.03.030.

587 [6] R. Sagl, A. Jarosik, D. Stifter, G. Angeli, The role of surface oxides on annealed high-strength steels in
588 hot-dip galvanizing, Corros. Sci. 70 (2013) 268-275. https://doi.org/10.1016/j.corsci.2013.01.039.

589 [7] M.-L. Giorgi, J. Diawara, S. Chen, A. Koltsov, J.-M. Mataigne, Influence of annealing treatment on
590 wetting of steels by zinc alloys, J. Mater. Sci. 47 (2012) 8483-8495. https://doi.org/10.1007/s10853-012-
591 6696-4.

592 [8] S. Swaminathan, M. Spiegel, Thermodynamic and kinetic aspects on the selective surface oxidation of
593 binary, ternary and quarternary model alloys, Appl. Surf. Sci. 253 (2007) 4607-4619.
594 https://doi.org/10.1016/j.apsusc.2006.10.031.

595 [9] N. Ruscassier, L. Gong, M. Ayouz, T. Reiss, P. Haghi-Ashtiani, M.-L. Giorgi, Selective oxidation of Fe-
596 Mn (1 wt. %) binary alloy, in: Galvatech 2017: 11th Int. Conf. on Zinc and Zinc Alloy Coated Sheet Steels,
597 Iron and Steel Institute of Japan, Tokyo, 2017, pp. 378-384.

598 [10] M. Pourmajidian, J.R. McDermid, Selective oxidation of a 0.1C-6Mn-2Si third generation advanced
599 high-strength steel during dew-point controlled annealing, Metall. Mater. Trans. A 49A (2018) 1795-1808.
600 https://doi.org/10.1007/s11661-018-4513-7.

601 [11] K. Shinoda, T. Yamamoto, S. Suzuki, Characterization of selective oxidation of manganese in surface
602 layers of Fe-Mn alloys by different analytical methods, ISIJ Int. 53 (2013) 2000-2006.
603 https://doi.org/10.2355/isijinternational.53.2000.

[12] V.F.C. Lins, L. Madeira, J.M.C. Vilela, M.S. Andrade, V.T.L. Buono, J.P. Guimaraes, E.A. Alvarenga, Selective oxidation of dual phase steel after annealing at different dew points, Appl. Surf. Sci. 257 (2011) 5871-5878. https://doi.org/10.1016/j.apsusc.2011.01.126.

[13] J.H. Bott, H. Yin, S. Sridhar, M. Auinger, Theoretical and experimental analysis of selective oxide and nitride formation in Fe-Al alloys, Corros. Sci. 91 (2015) 37-45. https://doi.org/10.1016/j.corsci.2014.10.024.

[14] A. Ollivier-Leduc, M.-L. Giorgi, D. Balloy, J.-B. Guillot, Study of selective oxidation by means of glow discharge optical emission spectroscopy, Corros. Sci. 53 (2011) 1375-1382. https://doi.org/10.1016/j.corsci.2011.01.012.

[15] M. Norden, M. Blumenau, T. Wuttke, K.-J. Peters, The change of steel surface chemistry regarding oxygen particle pressure and dew point, Appl. Surf. Sci. 271 (2013) 19-31. https://doi.org/10.1016/j.apsusc.2012.12.103.

[16] L.B. Liu, G.R. Jiang, H.Q. Wang, H.X. Teng, Effect of dew point during heating on selective oxidation of TRIP steels, Metall. Res. Technol. 114 (2017) 609. https://doi.org/10.1051/metal/2017070.

[17] G. Wu, J. Zhang, Effect of water pressure and soaking time on the selective oxidation of DP980 advanced high strength steel, Appl. Surf. Sci. 453 (2018) 252-262. https://doi.org/10.1016/j.apsusc.2018.05.034.

[18] S.H. Ham, C. Carteret, J. Angulo, G. Fricout, Relation between emissivity evolution during annealing and selective oxidation of TRIP steel, Corros. Sci. 132 (2018) 185-193. https://doi.org/10.1016/j.corsci.2017.12.032.

[19] X.S. Li, S.-I. Beak, C.-S. Oh, S.-J. Kim, Y.-W. Kim, Dew-point controlled oxidation of Fe-C-Mn-Al-Si-Cu transformation-induced plasticity-aided steels, Scr. Mater. 59 (2008) 290-293. https://doi.org/10.1016/j.scriptamat.2008.03.025.

[20] S. Chen, Influence de l'orientation des grains de ferrite sur l'oxydation sélective de l'acier, Ph.D thesis, École Centrale Paris, Paris, 2012 (in French).

[21] H.K. Mehtani, M.I. Khan, A. Durgaprasad, S.K. Deb, S. Parida, M.J.N.V. Prasad, D. Fullwood, R.D. Doherty, I. Samajdar, Oxidation behavior of interstitial free steel: The defining role of substrate crystallographic texture, Acta Mat. 190 (2020) 43-57.

[22] X. Vanden Eynden, J.-P. Servais, M. Lamberigts, Thermochemical surface treatment of iron-silicon and iron-manganese alloys, Surf. Interface Anal. 33 (2002) 322-329. https://doi.org/10.1002/sia.1198

[23] C. Martinez, R. Cremer, D. Loison, J.P. Servais, In-situ investigation on the oxidation behaviour of low alloyed steels annealed under N_2-5%H_2 protective atmosphere, Steel Res. 72 (2001) 508-511. https://doi.org/10.1002/srin.200100159.

[24] L. Gong, N. Ruscassier, M. Ayouz, P. Haghi-Ashtiani, M.-L. Giorgi, Analytical model of selective external oxidation of Fe-Mn binary alloys during isothermal annealing treatment, Corros. Sci. 166 (2020) 108454. https://doi.org/10.1016/j.corsci.2020.108454.

[25] C. Martinez, R. Cremer, D. Neuschütz, A. von Richthofen, In-situ surface analysis of annealed Fe-1.5%Mn and Fe-0.6%Mn low alloy steels, Anal. Bioanal. Chem. 374 (2002) 742-745. https://doi.org/10.1007/s00216-002-1538-x.

[26] T.B. Massalski, H.S. Okamoto, P.R. Subramanian, L. Kacprzak, Binary Alloy Phase Diagrams, Second ed., ASM International, Ohio, 1990.

[27] A.R. Troiano, F.T. McGuire, A study of the iron-rich iron-manganese alloys, Trans. ASM 31 (1943) 340-359.

[28] D. Huin, P. Flauder, J.-B. Leblond, Numerical simulation of internal oxidation of steels during annealing treatments, Oxid. Met. 64 (2005) 131-167. https://doi.org/10.1007/s11085-005-5718-x.

[29] C.T. Rueden, J. Schindelin, M.C. Hiner, B.E. DeZonia, A.E. Walter, E.T. Arena, K.W. Eliceir, *ImageJ2*: *ImageJ* for the next generation of scientific image data, BMC Bioinformatics 18 (2017) 529. https://doi.org/10.1186/s12859-017-1934-z.

[30] C.A. Schneider, W.S. Rasband, K.W. Eliceiri, NIH image to *ImageJ*: 25 years of image analysis, Nature Methods 9(7) (2012) 671-675. https://doi.org/10.1038/nmeth.2089.

[31] F. Li, H. Liu, W, Shi, L. Li, Thermodynamic consideration on selective surface oxidation of high strength steels prior to hot-dip galvanizing, J. Coat. Technol. Res. 8(5) (2011) 639-647. https://doi.org/10.1007/s11998-011-9334-1.

[32] J.W. Christian, The classical theory of nucleation, in: J.W. Christian (Eds.), Theory of Transformations in Metals and Alloys, Part I, Equilibrium and General Kinetic Theory, Pergamon Press, Oxford, 1975, pp. 418-475.

[33] E. Clouet, Modeling of nucleation processes, in: D.U. Furrer, S.L. Semiatin (Eds.), ASM Handbook Volume 22A: Fundamentals of Modelling for Metals Processing, ASM international, Ohio, 2009, pp. 203-219.

[34] A.Z. Hed, D.S. Tannhauser, Contribution to the Mn-O phase diagram at high temperature, J. Electrochem. Soc. 114 (1967) 314-318. https://doi.org/10.1149/1.2426584.

[35] P. Kofstad, Defects and diffusion in MnO, J. Phys. Chem. Solids 9 (1983) 879-889. https://doi.org/10.1016/0022-3697(83)90126-9.

[36] I. Bransky, N.M. Tallan, A gravimetric study of nonstoichiometric MnO, J. Electrochem. Soc. 118 (1971) 788-793. https://doi.org/10.1149/1.2408165.

668 [37] A.N. Grundy, B. Hallstedt, L.J. Gauckler, Assessment of the Mn-O system, J. Phase Equilibria. 24(1)
669 (2003) 21-39. https://doi.org/10.1007/s11669-003-0004-6.

670 [38] J.P. Novak, S. Labik, I. Malijevska, Chemical equilibrium, in: J.P. Novak, S. Labik, I. Malijevska
671 (Eds.), Physical Chemistry in Brief, Institute of Chemical Technology, Prague, 2005, pp. 226-261.

672 [39] D. Sonntag, Important values of the physical constants of 1986, vapor pressure formations based on the
673 ITS-90, and psychrometer formulae, Z. Meteorol 70 (1990) 340-344.

674 [40] W.-H. Hung, J. Schwartz, S. L. Bernasek, Sequential oxidation of Fe(100) by water adsorption:
675 formation of an ordered hydroxylated surface, Surf. Sci. 248 (1991) 332-342. https://doi.org/10.1016/0039-
676 6028(91)91179-2.

677 [41] D. J. Dwyer, G. W. Simmons, A study of the initial reaction of water vapor with Fe(001) surface, Surf.
678 Sci. 64 (1977) 617-632. https://doi.org/10.1016/0039-6028(77)90066-8.

679 [42] W.-H. Hung, J. Schwartz, S.L. Bernasek, Adsorption of H_2O on oxidized Fe(100) surfaces: comparison
680 between the oxidation of iron by H_2O and O_2, Surf. Sci. 294 (1993) 21-32. https://doi.org/10.1016/0039-
681 6028(93)90155-D.

682 [43] D.J. Dwyer, S.R. Kelemen, A. Kaldor, The water dissociation reaction on clean and oxidized iron (110),
683 J. Chem. Phys. 76 (1982) 1832-1837. https://doi.org/10.1063/1.443154.

684 [44] P. Jiang, M.W. Zappone, S.L. Bernasek, Interaction of water with clean and gallium precovered Fe(111)
685 surfaces, J. Vac. Sci. Technol. A 14 (1996) 2372-2377. https://doi.org/10.1116/1.580025.

686 [45] C. Wagner, Reaktionstypen bei der oxydation von legierungen, Zeitschrift fur Elcktrochemie 63 (1959)
687 772-782. https://doi.org/10.1002/bbpc.19590630713.

688 [46] R.A. Rapp, Kinetics, microstructures and mechanism of internal oxidation -- its effect and prevention in
689 high temperature alloy oxidation, Corros. 21 (1965) 382-401. https://doi.org/10.5006/0010-9312-21.12.382.

690 [47] R.A. Rapp, The transition from internal to external oxidation and the formation of interruption bands in
691 silver-indium alloys, Acta Metall. 9 (1961) 730-741. https://doi.org/10.1016/0001-6160(61)90103-1.

692 [48] J.-B. Leblond, M. Pignol, D. Huin, Predicting the transition from internal to external oxidation of alloys
693 using an extended Wagner model, Comptes Rendus Mécanique 341 (2013) 314-322.
694 https://doi.org/10.1016/j.crme.2013.01.003.

695 [49] J.J. Valencia, P.N. Quested, Thermophysical properties, in: S. Viswanathan, D. Apelian, R.J. Donahue,
696 B. DasGupta, M. Gywn, J.L. Jorstad, R.W. Monroe, M. Sahoo, T.E. Prucha, D. Twarog (Eds.), ASM
697 Handbook Volume 15: Casting, ASM international, Ohio, 2008, pp. 468-481.

698 [50] E.D. Williams, Surface steps and surface morphology: understanding macroscopic phenomena from
699 atomic observations, Surf. Sci. 299/300 (1994) 502-524. https://doi.org/10.1016/0039-6028(94)90678-5.

[51] C. Zhang, A.J. Gellman, M.H. Farias, G.A. Somorjai, The adsorbate induced faceting of the Mo(111) surface, Mat. Res. Bull. 20 (1985) 1129-1135. https://doi.org/10.1016/0025-5408(85)90086-8.

[52] N.J. Taylor, A low energy electron diffraction study of the structural effect of oxygen on the (111) face of a tungsten crystal, Surf. Sci. 2 (1964) 544-552. https://doi.org/10.1016/0039-6028(64)90098-6.

[53] J.C. Tracy, J.M. Blakely, A study of faceting of tungsten single crystal surfaces, Surf. Sci. 13 (1969) 313-336. https://doi.org/10.1016/0039-6028(69)90194-0.

[54] H.-C. Jeong, E.D. Williams, Steps on surfaces: experiment and theory, Surf. Sci. Rep. 34 (1999) 171-294. https://doi.org/10.1016/S0167-5729(98)00010-7.

[55] M.J.S. Spencer, A. Hung, I.K. Snook, I. Yarovsky, Density functional theory study of the relaxation and energy of iron surfaces, Surf. Sci. 513 (2002) 389-398. https://doi.org/10.1016/S0039-6028(02)01809-5.

[56] W.D. Kaplan, D. Chatain, P. Wynblatt, W.C. Carter, A review of wetting versus adsorption, complexions, and related phenomena: the Rosetta stone of wetting, J. Mater. Sci. 48 (2013) 5681-5717. https://doi.org/10.1007/s10853-013-7462-y.

[57] J.-P. Morniroli, Données Cristallographiques des Principaux Métaux et Métaloïdes, Techniques de l'Ingénieur, Saint-Denis Cedex, M4050, 2009.

[58] J. Weissmüller, Thermodynamic of nanocrystalline solids, in: P. Knauth, J. Schoonman (Eds), Nanocrystalline Metals and Oxides Selected Properties and Applications, Kluwer Academic Publishers, New York, 2002, pp. 1-39.

[59] R.V. Zucker, D. Chatain, U. Dahmen, S. Hagége, W.C. Carter, New software tools for the calculation and display of isolated and attached interfacial-energy minimizing particle shapes, J. Mater. Sci. 47 (2012) 8290-8302. https://doi.org/10.1007/s10853-012-6739-x.

[60] H. Sadan, W.D. Kaplan, Morphology and orientation of the equilibrated Au-sapphire $(10\bar{1}0)$ interface, J. Mater. Sci. 41 (2006) 5371-5375. https://doi.org/10.1007/s10853-006-0407-y.

[61] H. Sadan, W.D. Kaplan, Au-Sapphire (0001) solid-solid interfacial energy, J. Mater. Sci. 41 (2006) 5099-5107. https://doi.org/10.1007/s10853-006-0437-5.

[62] S. Curiotto, H. Chien, H. Meltzman, P. Wynblatt, G.S. Rohrer, W.D. Kaplan, D. Chatain, Orientation relationships of copper crystals on c-plane sapphire, Acta Mater. 59 (2011) 5320-5331. https://doi.org/10.1016/j.actamat.2011.05.008.

[63] S. Curiotto, H. Chien, H. Meltzman, S. Labat, P. Wynblatt, G.S. Rohrer, W.D. Kaplan, D. Chatain, Copper crystals on the $(11\bar{2}0)$ sapphire: orientation relationship, triple line ridges and interface shape equilibrium, J. Mater. Sci. 48 (2013) 3013-3026. https://doi.org/10.1007/s10853-012-7080-0.

731 [64] D. Chatain, V. Ghetta, P. Wynblatt, Equilibrium shape of copper crystals grown on sapphire, Interface
732 Sci. 12 (2004) 7-18. https://doi.org/10.1023/B:INTS.0000012290.07441.a8.

733 [65] R.J. Borg, G.J. Dienes, Point defects in elemental crystalline substances, in: R.J. Borg, G.J. Dienes
734 (Eds.), An Introduction to Solid State Diffusion, Academic Press, Cambridge, 1988, pp. 25-52.

735 [66] B.B. Kine, G.H. Redlich Rohm, The role of surfactants in emulsion polymerization, in: D.T. Wasan,
736 M.E. Ginn, D.O. Shah (Eds.), Surfactants in Chemical / Process Engineering, CRC Press, Floride, 1988, pp.
737 39-49.
738

Fig. 1 Temperature profiles for annealing experiments. The representative profile for continuous industrial annealing is shown by line 9; The heat treatment is interrupted during heating (lines 1-7) and during holding (lines 8-13) to study the nucleation and growth of selective oxides.

Fig. 2 EBSD maps obtained on the Fe-Mn alloys annealed at (a) 680 and (b) 700 °C during heating and at (c) 800 °C for 60 s during isothermal holding. The crystallographic planes shown are parallel to the alloy surface. The ferrite surface was not completely recrystallized at 680 °C and well recrystallized from 700 °C.

Fig. 3 Nucleation of oxide particles on Fe-Mn (1 wt. %) alloy in N_2-H_2 (5 vol. %), dew point -40 °C. (a) The oxide particles appear at 650 °C (temperature profile 1 in Fig. 1), mainly within the grain boundaries (white arrows, SEM). (b) Very small oxide particles appear at 680 °C (temperature profile 2 in Fig. 1) on some ferrite grains only (AFM).

Fig. 4 SEM images obtained on (a) Fe{100}, (b) Fe{110} and (c) Fe{111} of Fe-Mn (1 wt. %) alloy annealed at 700 °C in N_2-H_2 (5 vol. %), dew point -40°C. Numerous oxide particles a few tens of nanometers in size are present on the three ferrite grain orientations.

Fig. 5 AFM images obtained on (a) Fe{100}, (b) Fe{110} and (c) Fe{111} of Fe-Mn (1 wt. %) alloy annealed at 700 °C in N_2-H_2 (5 vol. %), dew point -40 °C. The mean equivalent diameter of the oxide particles depends on the ferrite grain orientation and increases in the following order of Fe{100} < Fe{111} < Fe{110}.

Fig. 6 EDX mapping of (d), (e) and (f) O, (g), (h) and (i) Mn, (j), (k) and (l) Fe and (a), (b) and (c) O-Mn-Fe all together obtained on (a), (d), (g) and (j) Fe{100}, (b), (e), (h) and (k) Fe{110}, and (c), (f), (i) and (l) Fe{111} of Fe-Mn (1 wt. %) alloy annealed at 700 °C in N_2-H_2 (5 vol.%), dew point -40 °C. All the particles contain mainly Mn and O in the same atomic proportions.

Fig. 7 EDX mapping of (d), (e) and (f) O, (g), (h) and (i) Mn, (j), (k) and (l) Fe and (a), (b) and (c) O-Mn-Fe all together obtained on (a), (d), (g) and (j) Fe{100}, (b), (e), (h) and (k) Fe{110}, and (c), (f), (i) and (l) Fe{111} of Fe-Mn (1 wt. %) alloy annealed at 800 °C for 60 s in N_2-H_2 (5 vol. %), dew point -40 °C. All the particles contain mainly Mn and O in the same atomic proportions, i.e., 48.9 at. % Mn, 50.6 at. % O and 0.5 at. % Fe (•, Fig. 7(a)), 47.7 at. % Mn, 50.8 at. % O and 1.5 at. % Fe (•, Fig. 7(b)) and 46.7 at. % Mn, 43.2 at. % O and 0.1 at. % Fe (•, Fig. 7(c)).

Fig. 8 EDX mapping of (d), (e) and (f) O, (g), (h) and (i) Mn, (j), (k) and (l) Fe and (a), (b) and (c) O-Mn-Fe all together obtained on (a), (d), (g) and (j) Fe{100}, (b), (e), (h) and (k) Fe{110}, and (c), (f), (i) and (l) Fe{111} of Fe-Mn (1 wt. %) alloy annealed at 800 °C for 120 s in N_2-H_2 (5 vol. %), dew point -40 °C. All the particles contain mainly Mn and O in the same atomic proportions, i.e. 57.7 at. % Mn, 38.8 at. % O and 3.5 at. % Fe (•, Fig. 8(a)), 51.4 at. % Mn, 48.5 at. % O and 0.1 at. % Fe (•, Fig. 8(b)) and 57.8 at. % Mn, 41.6 at. % O and 0.6 at. % Fe (•, Fig. 8(c)).

Fig. 9 SEM images obtained on Fe{100} (left column), Fe{110} (middle column) and Fe{111} (right column) of Fe-Mn (1 wt. %) alloy annealed at (a), (b) and (c) 750 and (d), (e) and (f) 800 °C during heating and at 800 °C for (g), (h) and (i) 60, (j), (k) and (l) 120, (m), (n) and (o)180, (p), (q) and (r) 240 and (s), (t) and (u) 300 s during isothermal holding, in N_2-H_2 (5 vol. %), dew point -40 °C.

Fig. 10 Characteristic geometrical parameters of the oxides formed on Fe{100} (red line), Fe{110} (green line) and Fe{111} (blue line), namely the surface density n_{oxides} (a), the mean equivalent diameter D_{eq} (b), the surface area fraction covered A_f (c) and the maximum height H (d), as a function of the annealing step (temperature-time) in N_2-H_2 (5 vol. %), dew point -40 °C. The diamond points in Fig. 10(d) are the values measured with STEM images on cross-sections of the samples (as in Figs. 7 and 8).

Fig. 11 AFM images obtained on Fe{100} (left column), Fe{110} (middle column) and Fe{111} (right column) of Fe-Mn (1 wt. %) alloy annealed at (a), (b) and (c) 750 and (d), (e) and (f) 800 °C during heating and at 800 °C for (g), (h) and (i) 60, (j), (k) and (l) 120, (m), (n) and (o)180, (p), (q) and (r) 240 and (s), (t) and (u) 300 s during isothermal holding, in N_2-H_2 (5 vol. %), dew point -40 °C.

Fig. 12 Height (H) as a function of lateral dimension (x) for individual oxide particles on Fe{100}, Fe{110} and Fe{111} of Fe-Mn (1 wt. %) alloy annealed at 800 °C for (a) 60, (b) 180 and (c) 300 s, in N_2-H_2 (5 vol. %), dew point -40 °C. The selected particles in Fig. 11 are marked by lines of the same colour as in this figure (red for Fe{100}, green for Fe{110} and blue for Fe{111}). The 0 of the x-axis corresponds to the left or upper side of the line in Fig. 11. The oxide particles on Fe{100} and Fe{111} are above the level of the ferrite substrate while they are more or less at the same level for Fe{110}.

Fig. 13 HAADF-STEM images obtained on the TEM samples from (a) and (d) Fe{100}, (b) and (e) Fe{110}, and (c) and (f) Fe{111} of Fe-Mn (1 wt. %) alloy annealed at 800 °C for (a-c) 60 s and (d-f) 120 s in N_2-H_2 (5 vol. %), dew point -40 °C. The maximum oxide height H' and the contact angle between ferrite and particles taken in the analysis are indicated by two parallel lines and the angular sector respectively.

Fig. 14 SEM images obtained on Fe{100} (left column), Fe{110} (middle column) and Fe{111} (right column) of Fe-Mn (1 wt. %) alloy annealed at 800 °C for (a), (b) and (c) 0 and (d), (e) and (f) 30, (g), (h) and (i) 60, (j), (k) and (l) 120, (m), (n) and (o)180, (p), (q) and (r) 240 and (s), (t) and (u) 300 s during isothermal holding, in N_2-H_2 (5 vol. %), dew point -40 °C.

Fig. 1 Temperature profiles for annealing experiments. The representative profile for continuous industrial annealing is shown by line 9; The heat treatment is interrupted during heating (lines 1-7) and during holding (lines 8-13) to study the nucleation and growth of selective oxides.

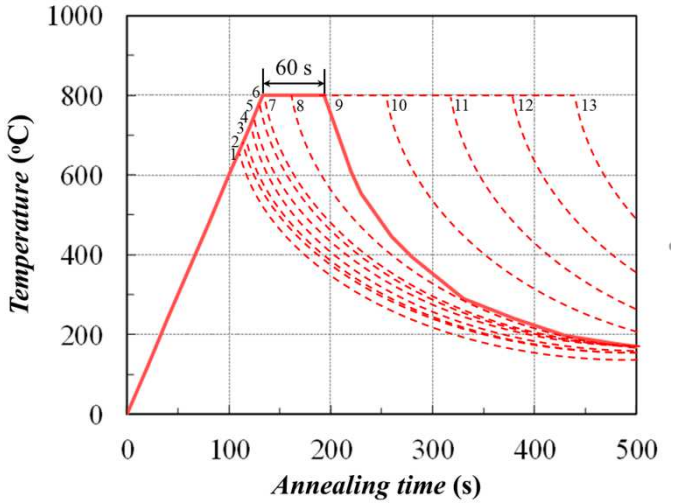

Fig. 2 EBSD maps obtained on the Fe-Mn alloys annealed at (a) 680 and (b) 700 °C during heating and at (c) 800 °C for 60 s during isothermal holding. The crystallographic planes shown are parallel to the alloy surface. The ferrite surface was not completely recrystallized at 680 °C and well recrystallized from 700 °C.

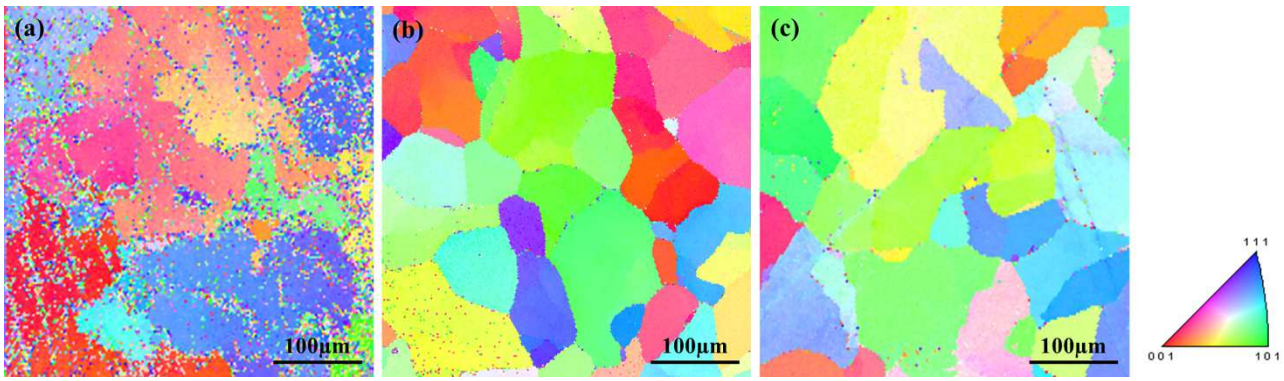

Fig. 3 Nucleation of oxide particles on Fe-Mn (1 wt. %) alloy in N_2-H_2 (5 vol. %), dew point -40 °C. (a) The oxide particles appear at 650 °C (temperature profile 1 in Fig. 1), mainly within the grain boundaries (white arrows, SEM). (b) Very small oxide particles appear at 680 °C (temperature profile 2 in Fig. 1) on some ferrite grains only (AFM).

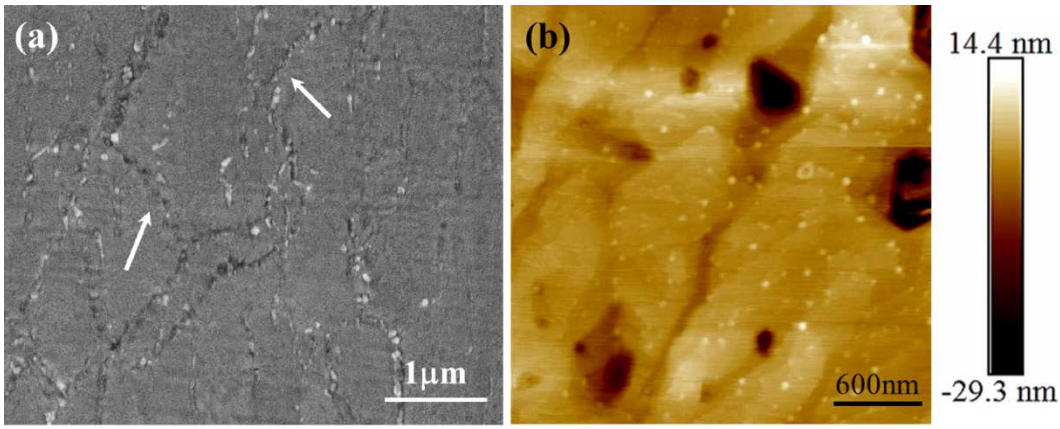

Fig. 4 SEM images obtained on (a) Fe{100}, (b) Fe{110} and (c) Fe{111} of Fe-Mn (1 wt. %) alloy annealed at 700 °C in N_2-H_2 (5 vol. %), dew point -40°C. Numerous oxide particles a few tens of nanometers in size are present on the three ferrite grain orientations.

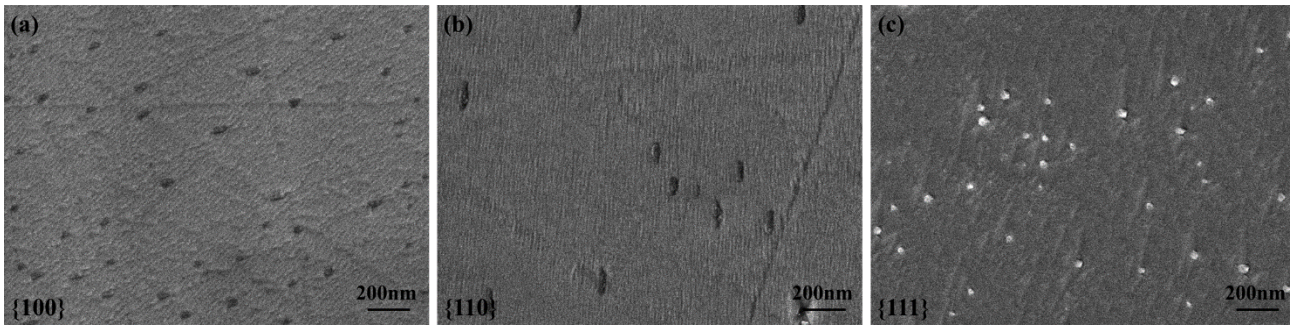

Fig. 5 AFM images obtained on (a) Fe{100}, (b) Fe{110} and (c) Fe{111} of Fe-Mn (1 wt. %) alloy annealed at 700 °C in N_2-H_2 (5 vol. %), dew point -40 °C. The mean equivalent diameter of the oxide particles depends on the ferrite grain orientation and increases in the following order of Fe{100} < Fe{111} < Fe{110}.

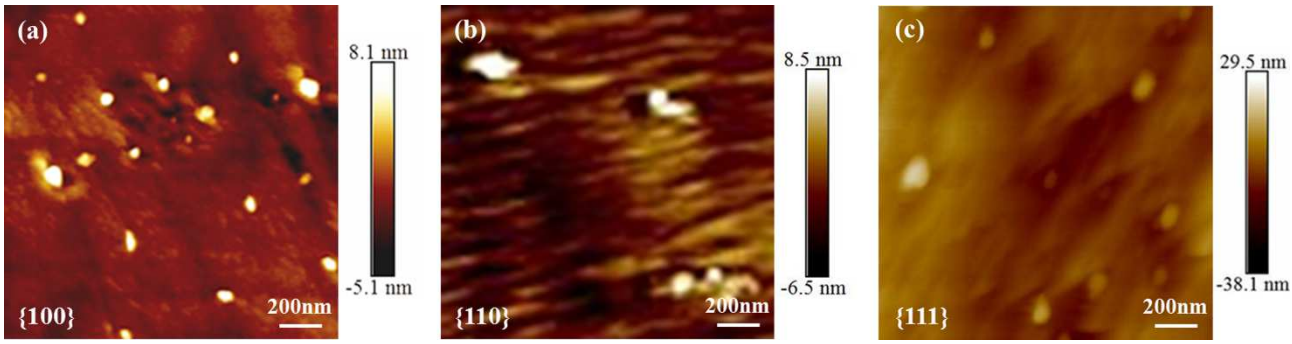

Fig. 6 EDX mapping of (d), (e) and (f) O, (g), (h) and (i) Mn, (j), (k) and (l) Fe and (a), (b) and (c) O-Mn-Fe all together obtained on (a), (d), (g) and (j) Fe{100}, (b), (e), (h) and (k) Fe{110}, and (c), (f), (i) and (l) Fe{111} of Fe-Mn (1 wt. %) alloy annealed at 700 °C in N_2-H_2 (5 vol. %), dew point -40 °C. All the particles contain mainly Mn and O in the same atomic proportions.

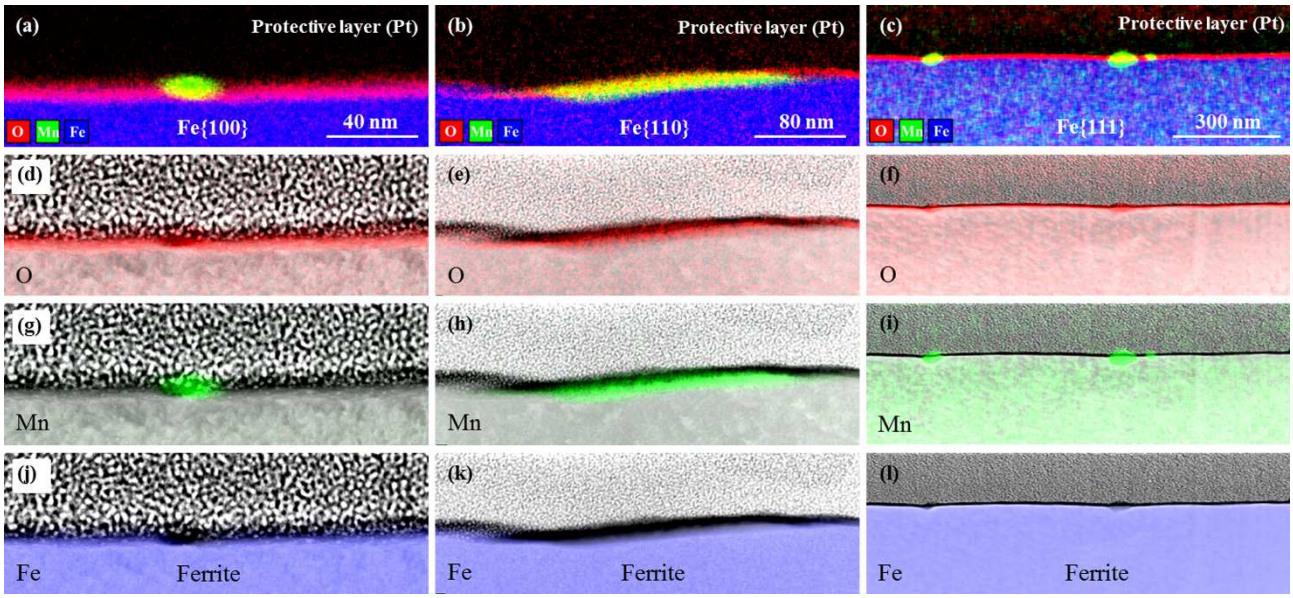

Fig. 7 EDX mapping of (d), (e) and (f) O, (g), (h) and (i) Mn, (j), (k) and (l) Fe and (a), (b) and (c) O-Mn-Fe all together obtained on (a), (d), (g) and (j) Fe{100}, (b), (e), (h) and (k) Fe{110}, and (c), (f), (i) and (l) Fe{111} of Fe-Mn (1 wt. %) alloy annealed at 800 °C for 60 s in N_2-H_2 (5 vol. %), dew point -40 °C. All the particles contain mainly Mn and O in the same atomic proportions, i.e., 48.9 at. % Mn, 50.6 at. % O and 0.5 at. % Fe (•, Fig. 7(a)), 47.7 at. % Mn, 50.8 at. % O and 1.5 at. % Fe (•, Fig. 7(b)) and 46.7 at. % Mn, 43.2 at. % O and 0.1 at. % Fe (•, Fig. 7(c)).

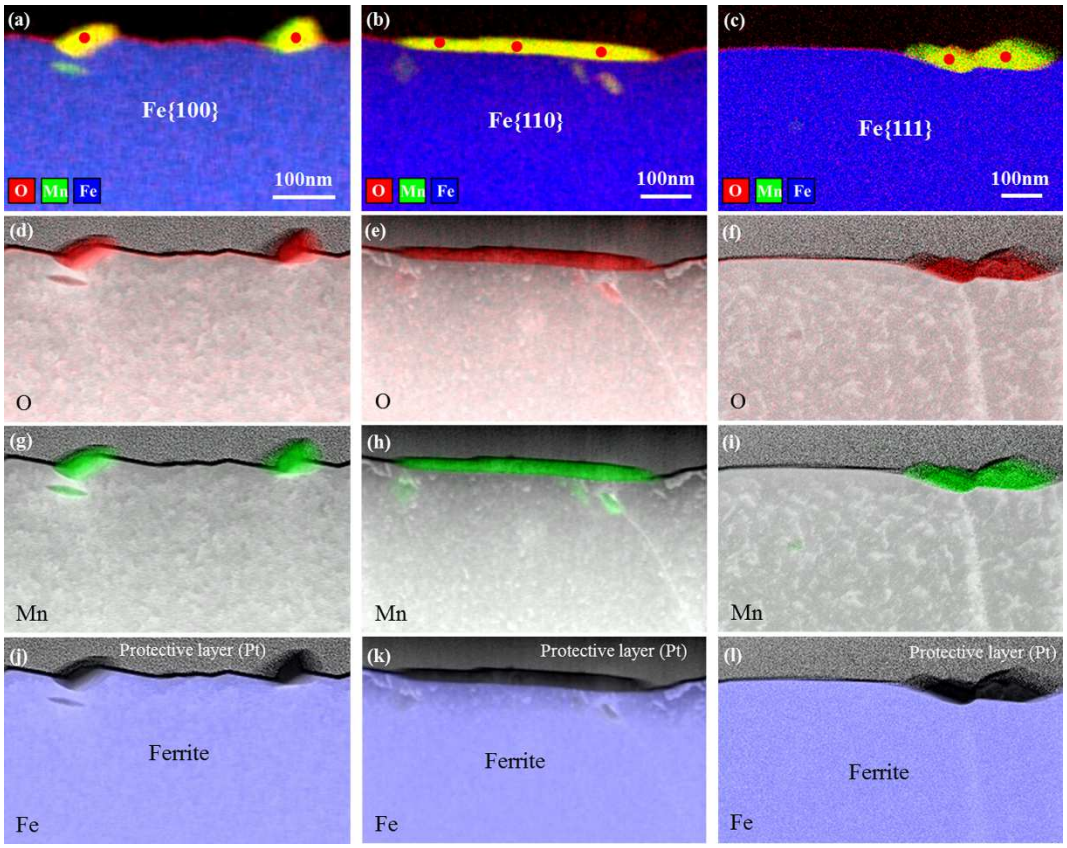

Fig. 8 EDX mapping of (d), (e) and (f) O, (g), (h) and (i) Mn, (j), (k) and (l) Fe and (a), (b) and (c) O-Mn-Fe all together obtained on (a), (d), (g) and (j) Fe{100}, (b), (e), (h) and (k) Fe{110}, and (c), (f), (i) and (l) Fe{111} of Fe-Mn (1 wt. %) alloy annealed at 800 °C for 120 s in N_2-H_2 (5 vol. %), dew point -40 °C. All the particles contain mainly Mn and O in the same atomic proportions, i.e. 57.7 at. % Mn, 38.8 at. % O and 3.5 at. % Fe (•, Fig. 8(a)), 51.4 at. % Mn, 48.5 at. % O and 0.1 at. % Fe (•, Fig. 8(b)) and 57.8 at. % Mn, 41.6 at. % O and 0.6 at. % Fe (•, Fig. 8(c)).

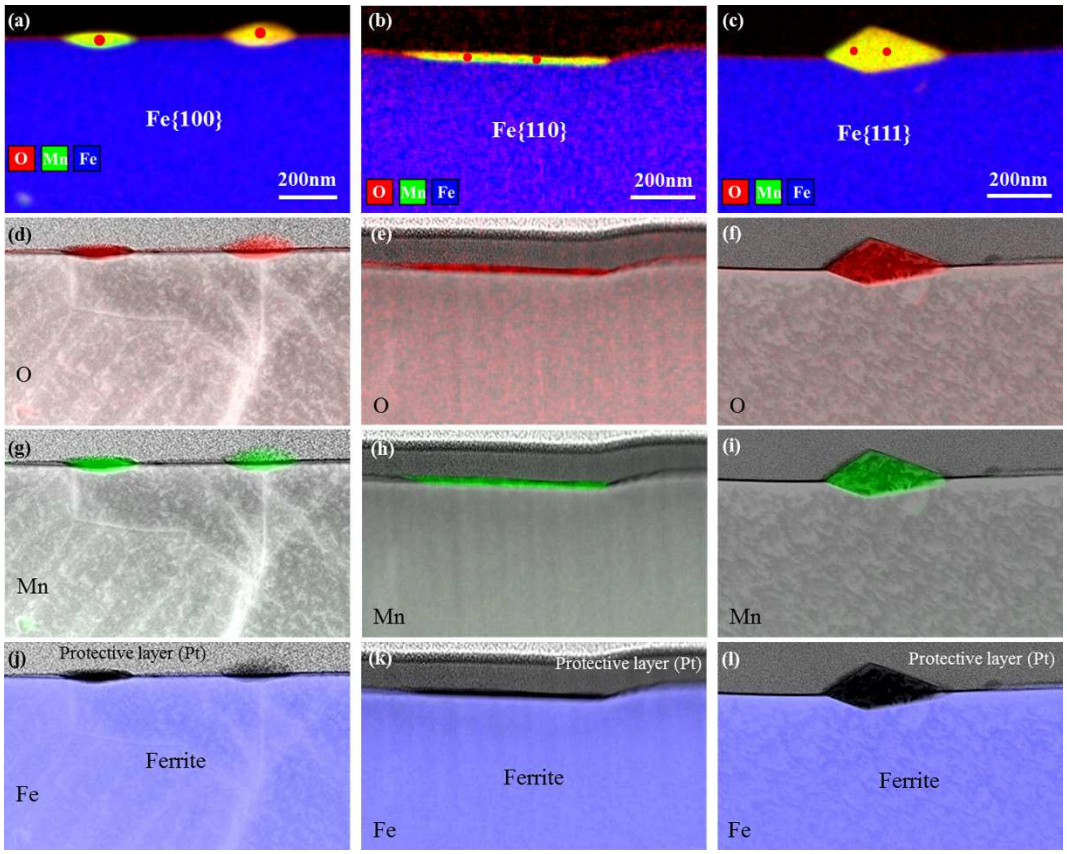

Fig. 9 SEM images obtained on Fe{100} (left column), Fe{110} (middle column) and Fe{111} (right column) of Fe-Mn (1 wt. %) alloy annealed at (a), (b) and (c) 750 and (d), (e) and (f) 800 °C during heating and at 800 °C for (g), (h) and (i) 60, (j), (k) and (l) 120, (m), (n) and (o)180, (p), (q) and (r) 240 and (s), (t) and (u) 300 s during isothermal holding, in N_2-H_2 (5 vol. %), dew point -40 °C.

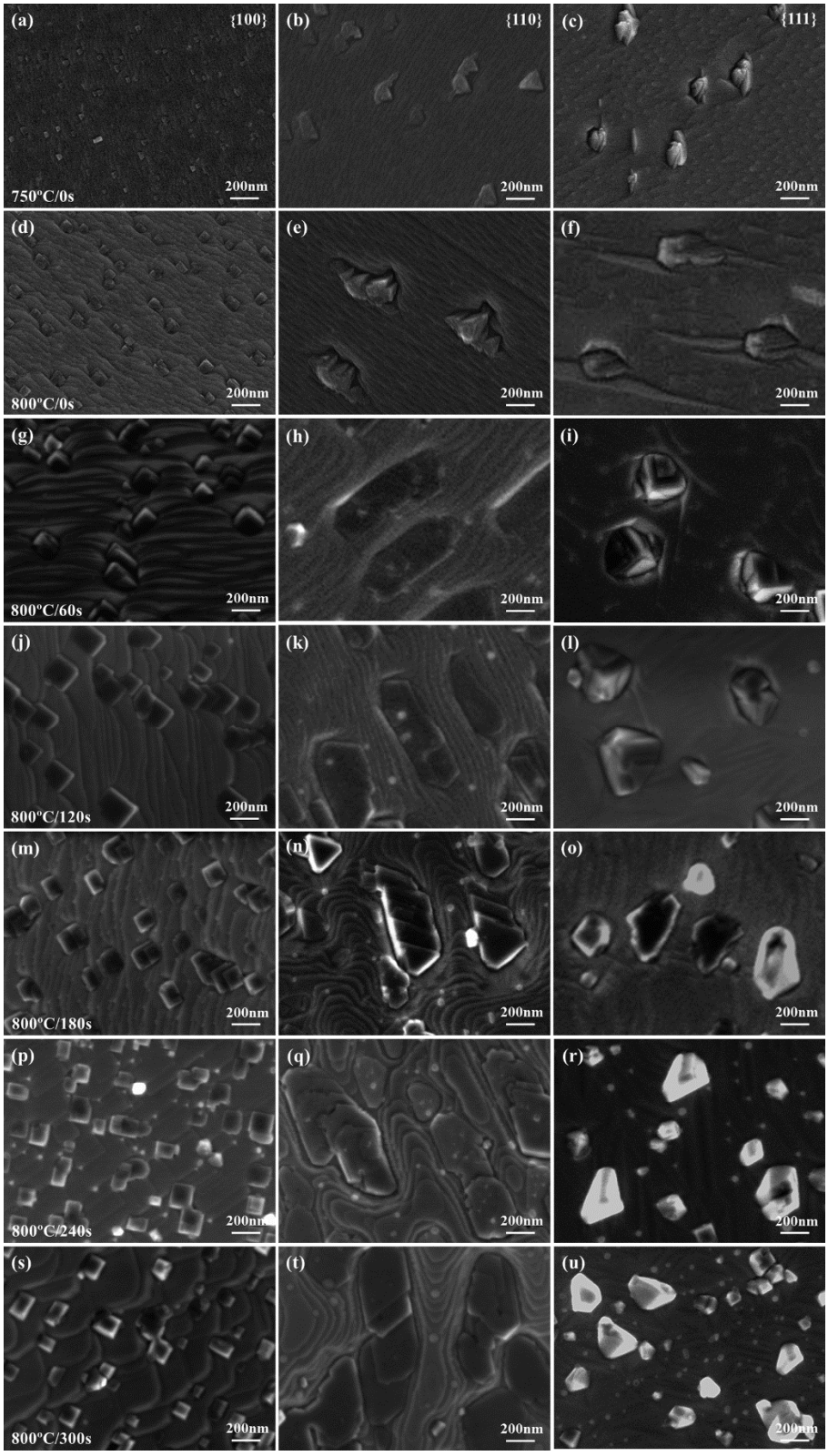

Fig. 10 Characteristic geometrical parameters of the oxides formed on Fe{100} (red line), Fe{110} (green line) and Fe{111} (blue line), namely the surface density n_{oxides} (a), the mean equivalent diameter D_{eq} (b), the surface area fraction covered A_f (c) and the maximum height H (d), as a function of the annealing step (temperature-time) in N_2-H_2 (5 vol. %), dew point -40 °C. The diamond points in Fig. 10(d) are the values measured with STEM images on cross-sections of the samples (as in Figs. 7 and 8).

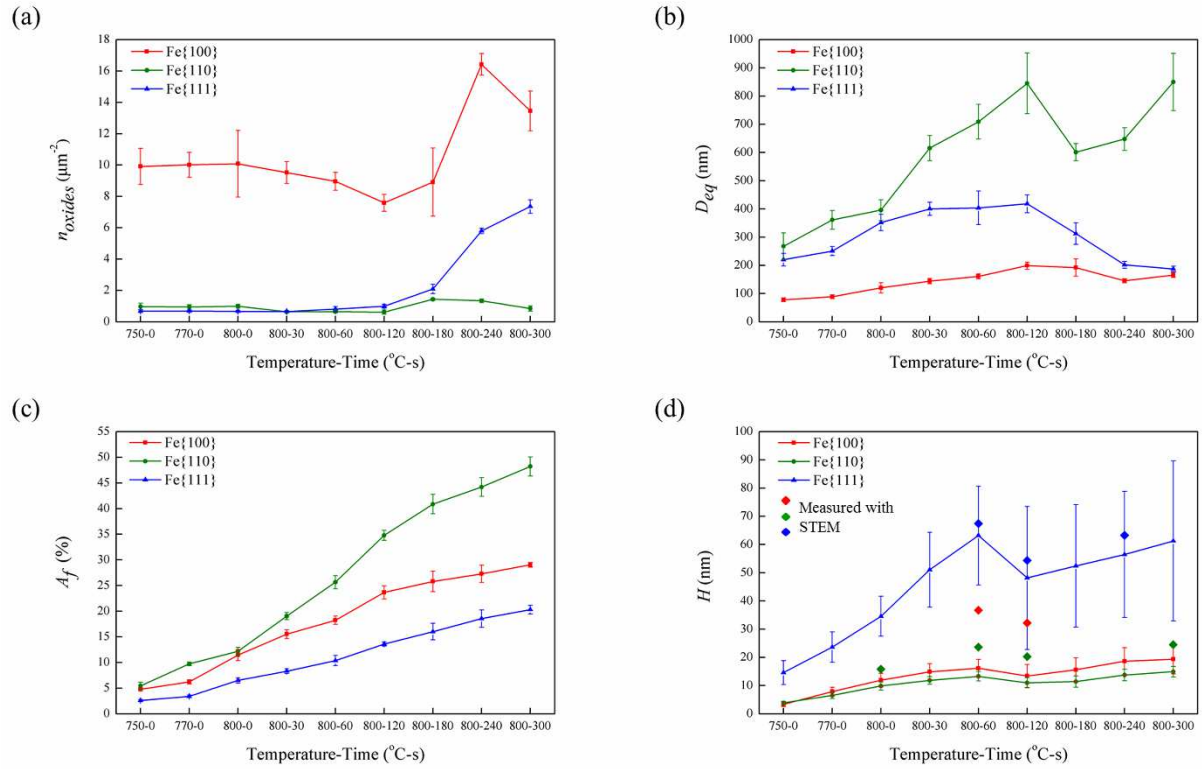

Fig. 11 AFM images obtained on Fe{100} (left column), Fe{110} (middle column) and Fe{111} (right column) of Fe-Mn (1 wt. %) alloy annealed at (a), (b) and (c) 750 and (d), (e) and (f) 800 °C during heating and at 800 °C for (g), (h) and (i) 60, (j), (k) and (l) 120, (m), (n) and (o)180, (p), (q) and (r) 240 and (s), (t) and (u) 300 s during isothermal holding, in N_2-H_2 (5 vol. %), dew point -40 °C.

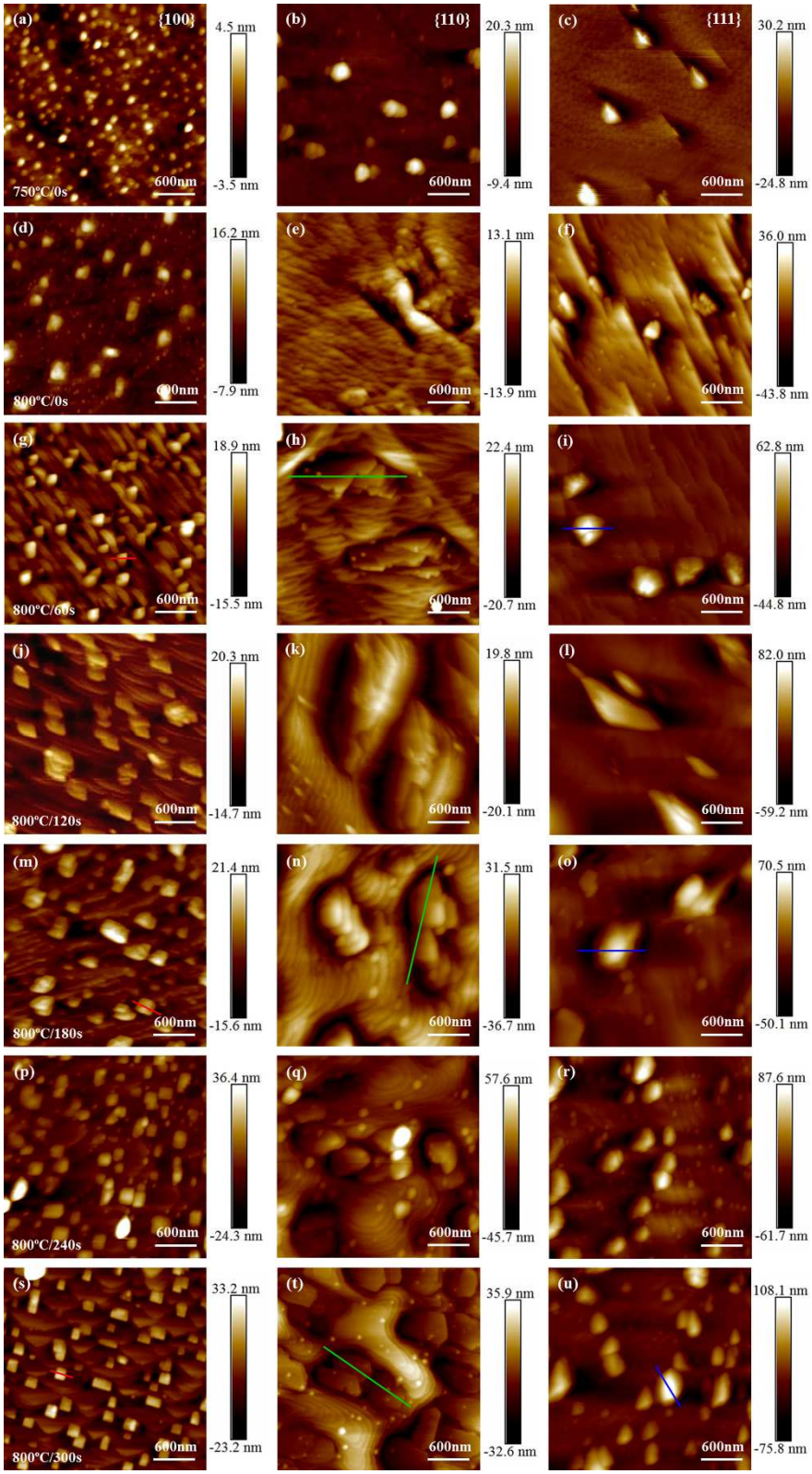

Fig. 12 Height (H) as a function of lateral dimension (x) for individual oxide particles on Fe{100}, Fe{110} and Fe{111} of Fe-Mn (1 wt. %) alloy annealed at 800 °C for (a) 60, (b) 180 and (c) 300 s, in N_2-H_2 (5 vol. %), dew point -40 °C. The selected particles in Fig. 11 are marked by lines of the same colour as in this figure (red for Fe{100}, green for Fe{110} and blue for Fe{111}). The 0 of the x-axis corresponds to the left or upper side of the line in Fig. 11. The oxide particles on Fe{100} and Fe{111} are above the level of the ferrite substrate while they are more or less at the same level for Fe{110}.

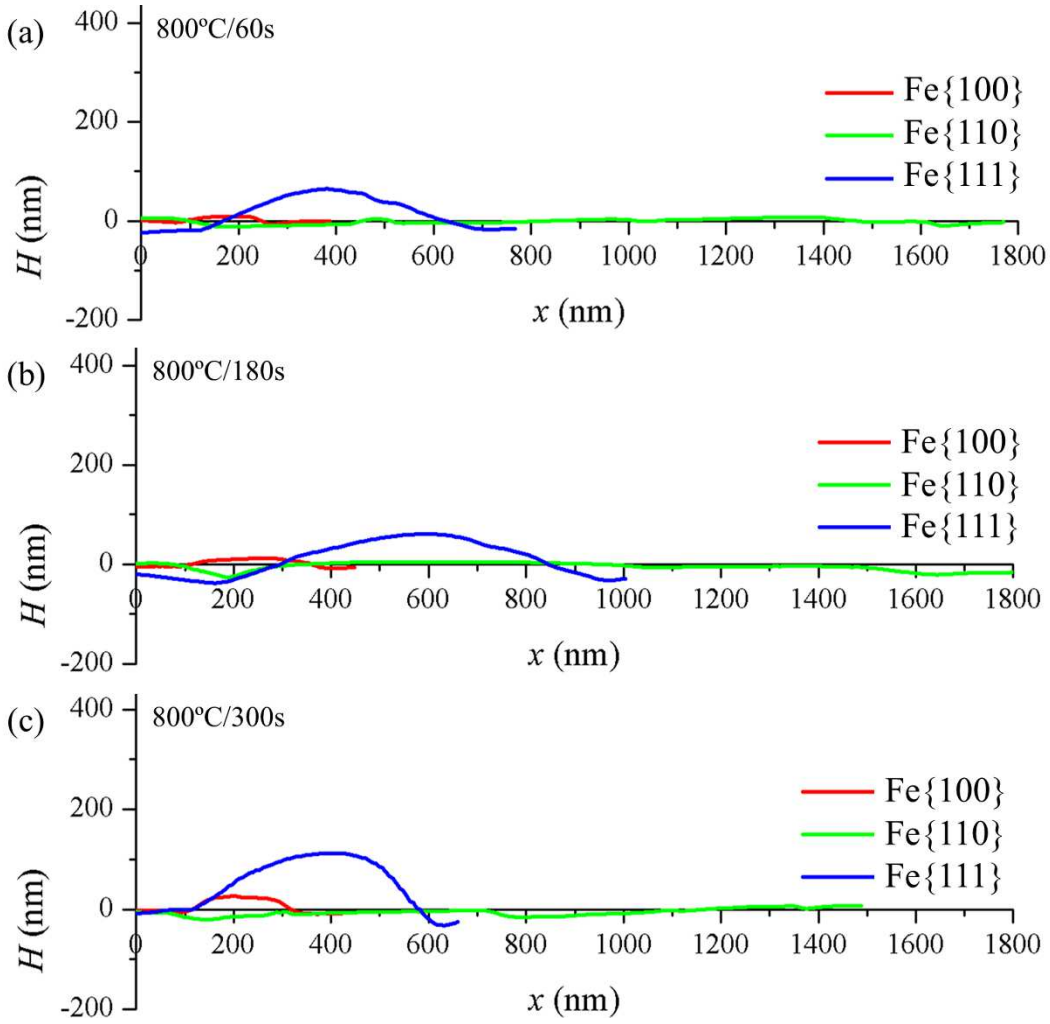

Fig. 13 HAADF-STEM images obtained on the TEM samples from (a) and (d) Fe{100}, (b) and (e) Fe{110}, and (c) and (f) Fe{111} of Fe-Mn (1 wt. %) alloy annealed at 800 °C for (a-c) 60 s and (d-f) 120 s in N_2-H_2 (5 vol. %), dew point -40 °C. The maximum oxide height *H'* and the contact angle between ferrite and particles taken in the analysis are indicated by two parallel lines and the angular sector respectively.

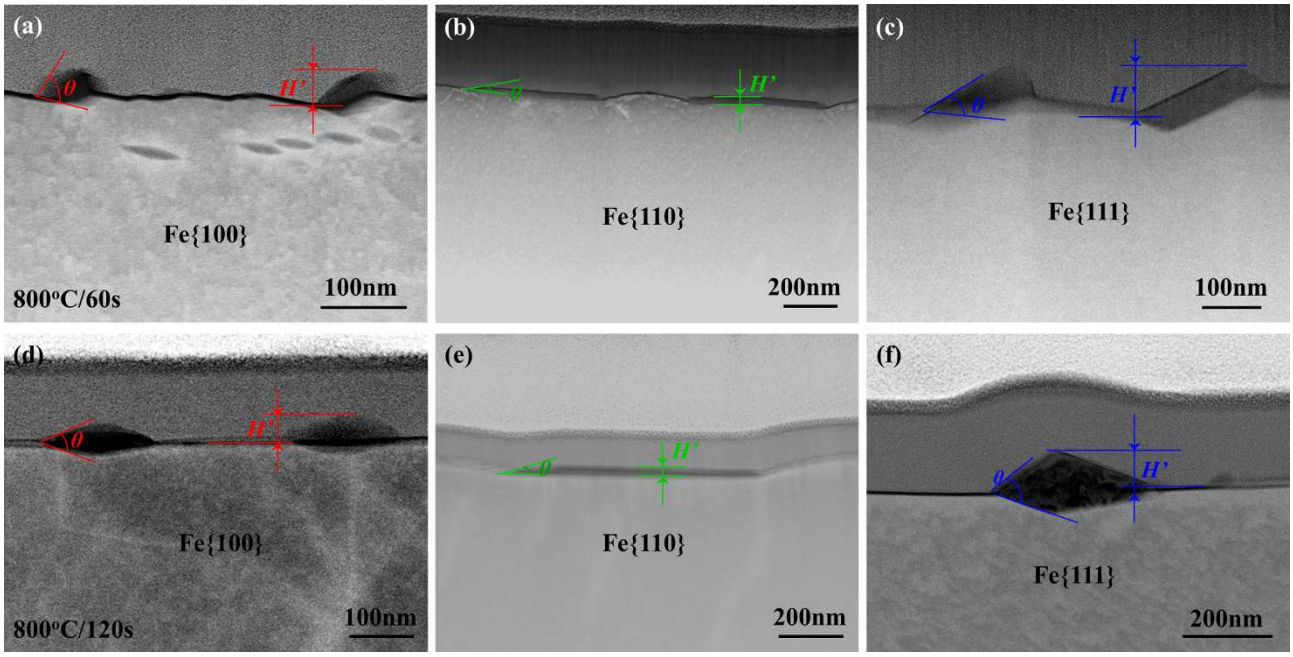

879 **Fig. 14** SEM images obtained on Fe{100} (left column), Fe{110} (middle column) and Fe{111} (right
880 column) of Fe-Mn (1 wt. %) alloy annealed at 800 °C for (a), (b) and (c) 0 and (d), (e) and (f) 30, (g), (h) and
881 (i) 60, (j), (k) and (l) 120, (m), (n) and (o)180, (p), (q) and (r) 240 and (s), (t) and (u) 300 s during isothermal
882 holding, in N_2-H_2 (5 vol. %), dew point -40 °C.

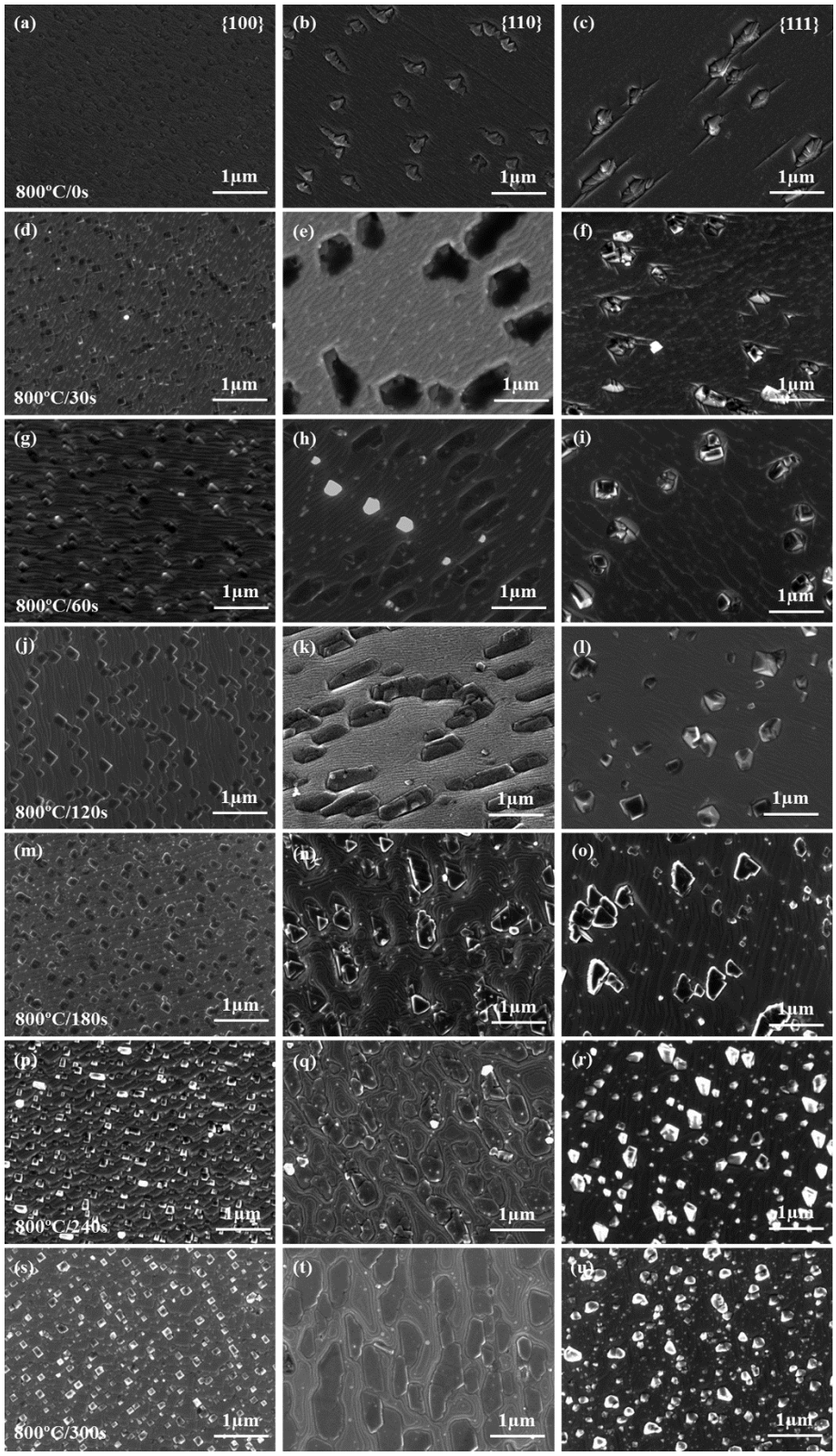

883